

See discussions, stats, and author profiles for this publication at: <https://www.researchgate.net/publication/305388493>

# Accurate quantitative phase digital holographic microscopy with single- and multiple-wavelength telecentric and nontelecentric configurations

Article in *Applied Optics* · July 2016

DOI: 10.1364/AO.55.005666

CITATIONS

0

READS

35

5 authors, including:



**Thanh Nguyen**

The Catholic University of America

9 PUBLICATIONS 2 CITATIONS

SEE PROFILE



**George Nehmetallah**

The Catholic University of America

68 PUBLICATIONS 206 CITATIONS

SEE PROFILE



**Scott Mathews**

The Catholic University of America

83 PUBLICATIONS 961 CITATIONS

SEE PROFILE

# Accurate quantitative phase digital holographic microscopy with single- and multiple-wavelength telecentric and nontelecentric configurations

THANH NGUYEN,<sup>1</sup> GEORGE NEHMETALLAH,<sup>1,\*</sup> CHRISTOPHER RAUB,<sup>2</sup> SCOTT MATHEWS,<sup>1</sup> AND ROLA AYLO<sup>3</sup>

<sup>1</sup>Electrical Engineering & Computer Science, Catholic University of America, Washington, DC 20064, USA

<sup>2</sup>Biomedical Engineering, Catholic University of America, Washington, DC 20064, USA

<sup>3</sup>Technical Advisor, Oblon, 1940 Duke Street, Alexandria, Virginia 22314, USA

\*Corresponding author: nehmetallah@cua.edu

Received 29 March 2016; accepted 13 June 2016; posted 17 June 2016 (Doc. ID 262122); published 18 July 2016

In this work, we investigate, both theoretically and experimentally, single-wavelength and multiwavelength digital holographic microscopy (DHM) using telecentric and nontelecentric configurations in transmission and reflection modes. A single-wavelength telecentric imaging system in DHM was originally proposed to circumvent the residual parabolic phase distortion due to the microscope objective (MO) in standard nontelecentric DHM configurations. However, telecentric configurations cannot compensate for higher order phase aberrations. As an extension to the telecentric and nontelecentric arrangements in single-wavelength DHM (SW-DHM), we propose multiple-wavelength telecentric DHM (MW-TDHM) in reflection and transmission modes. The advantages of MW-TDHM configurations are to extend the vertical measurement range without phase ambiguity and optically remove the parabolic phase distortion caused by the MO in traditional MW-DHM. These configurations eliminate the need for a second reference hologram to subtract the two-phase maps and make digital automatic aberration compensation easier to apply compared to nontelecentric configurations. We also discuss a reconstruction algorithm that eliminates the zero-order and virtual images using spatial filtering and another algorithm that minimizes the intensity of fluctuations using apodization. In addition, we employ two polynomial models using 2D surface fitting to compensate digitally for chromatic aberration (in the multiwavelength case) and for higher order phase aberrations. A custom-developed user-friendly graphical user interface is employed to automate the reconstruction processes for all configurations. Finally, TDHM is used to visualize cells from the highly invasive MDA-MB-231 cultured breast cancer cells. © 2016 Optical Society of America

**OCIS codes:** (090.1995) Digital holography; (100.3010) Image reconstruction techniques; (090.1000) Aberration compensation; (120.5050) Phase measurement; (090.2880) Holographic interferometry.

<http://dx.doi.org/10.1364/AO.55.005666>

## 1. INTRODUCTION

Quantitative phase digital holographic microscopy has had an enormous impact in the fields of living cells [1–7], neural science [8], cell and nanoparticle tracking [9,10], biophotonics and bioengineering [11,12], microfluidics [13], and metrology [14,15] because it can carry out quantitative, high-resolution, multiscale, real-time, 3D, and nondestructive analyses of biological processes. In addition, a digital holographic microscopy (DHM) system can be used to perform live 3D profilometry for the design and testing of microelectromechanical systems (MEMS) and components [16–18].

Traditional DHM systems record a digital hologram using a microscope objective (MO) [19–23]. One of the drawbacks of traditional DHM setups is that the object phase recovered from digital reconstruction using the Fresnel transform suffers from a

parabolic phase factor introduced by the MO. The phase of the MO is superposed over the object phase, often obscuring it. Also, the phase tilt introduced by the reference beam results in linear fringes with high frequency that also obscure the real phase of the object. DHM setups can be constructed using single-wavelength (SW) and multiwavelength (MW) sources. In a SW-DHM setup, one wavelength is used to record a single hologram on a CCD. In order to reconstruct the object phase accurately, the reconstruction parameters, which include the angle of the reference beam, the focal length of the MO, the object and image distances, and the reconstruction distance, have to be known with high precision [19,23]. Also, this setup has a limited height range of only a few wavelengths and sharp edges larger than a wavelength that are often difficult to decipher using phase unwrapping techniques [23,24]. On the other

hand, in MW-DHM, these parameters do not have to be measured with high precision, and depending on the beating synthetic wavelength, objects with heights much larger than a wavelength (in the tens of microns range) can be reconstructed without ambiguity [15,21,23]. The disadvantage of this setup is that it requires an elaborate alignment in which two separate lasers are often used (for capturing dynamic events and for synthetic wavelengths that ranges from 0.5 to 10  $\mu\text{m}$ ). Also, achromatic optics are required, and postprocessing is needed to align and scale the reconstructed phase images. It is worth mentioning that both techniques suffer from spatial fluctuations of the transmitted optical field which can be corrected with a digital aperture apodization such as a Gaussian, super-Gaussian or trigonometric function [25]. If the reconstruction parameters are measured with high precision, which is difficult in a laboratory setup, manual and automatic numerical phase compensation techniques can be employed to cancel phase aberrations inherent in the optical setup and the optical components of the system [26–30]. Phase aberrations can be due to (a) misalignment, (b) multiwavelength methods resulting in chromatic aberration, (c) the MO resulting in parabolic phase curvature, (d) the angle of the reference beam resulting in linear phase distortion, and (e) different optical components used in the setup, which may introduce additional spherical aberration, astigmatism, coma, or other distortions. One well-known manual technique is based on using a phase mask during reconstruction [26–28]; another technique uses automatic aberration compensation [29,30]. Both of these techniques require exact knowledge of the setup parameters to work. On the other hand, optical techniques (e.g., telecentric arrangements) [31–34] may be employed to compensate for both the parabolic phase curvature and the phase tilt, which constitute the bulk of the phase aberrations but fail to cancel chromatic aberration and higher order aberrations.

In this work, we discuss theoretically and experimentally single-wavelength and multiwavelength DHMs using nontelecentric (traditional) and telecentric configurations in reflection and transmission modes. Advantages and disadvantages of the different configurations are studied in detail. As an extension to the telecentric and nontelecentric arrangements in single-wavelength DHM (SW-DHM), we propose multiple-wavelength telecentric DHM (MW-TDHM) in reflection and transmission modes. SW/MW-TDHM configurations are used to reduce the number of reconstruction parameters, which are difficult to obtain with high accuracy in a laboratory setup. Also, in this paper, we not only use telecentric configurations to compensate for MO and reference beam phase aberrations optically but also perform surface fitting using two polynomial models to digitally create a phase mask that can compensate for both chromatic aberrations (in the multiwavelength case) and for higher order phase aberrations that are not corrected optically. In addition, reconstruction algorithms that eliminate the zero-order and virtual images using spatial filtering, and that minimize intensity and phase fluctuations using apodization, are also discussed. A custom-developed user-friendly graphical user interface (GUI) has been developed to automate the reconstruction processes for all configurations. Finally, cells from the highly invasive MDA-MB-231 breast cancer cell line

were cultured and TDHM was employed to reconstruct the amplitude and phase images from the recorded holograms.

This paper is divided as follows. In Section 2, a theoretical study of nontelecentric and telecentric SW-DHM is developed along with the different aberration compensation techniques. In Section 3, the theory of telecentric and nontelecentric multiwavelength DHM (MW-DHM) is discussed. In Section 4, experimental setups of the configurations previously considered in Sections 2 and 3 are constructed, the advantages and disadvantages of each configuration are discussed, and experimental results are obtained. The custom-developed GUI used to automate the recording and reconstruction process is also described in detail. Finally, we conclude with some remarks.

## 2. THEORETICAL STUDY OF NONTELECENTRIC AND TELECENTRIC SW-DHM

### A. Nontelecentric DHM Configuration (SW-DHM)

Digital holograms are generated by recording the interference pattern of two mutually coherent beams. These two beams are the object beam and the reference beam, and the recording medium is usually a CCD [15,21,23]. The digital hologram recorded on the CCD due to the interference of the object beam  $E_O$  and the reference beam  $E_R$  is given by

$$h(x, y) \propto I_H(x, y) = |E_R|^2 + |E_O|^2 + E_R^* E_O + E_O^* E_R, \quad (1)$$

where the \* notation denotes the complex conjugate.

A digital hologram  $h(k, l)$  is sampled along a two-dimensional array by the CCD camera as

$$h(k, l) = h(x, y) \text{rect}\left(\frac{x}{L}, \frac{y}{L}\right) \sum_{k=-\frac{N}{2}}^{\frac{N}{2}-1} \sum_{l=-\frac{N}{2}}^{\frac{N}{2}-1} \delta(x - k\Delta x, y - l\Delta y), \quad (2)$$

where  $(-\frac{N}{2} \leq k, l \leq \frac{N}{2} - 1)$ ,  $L \times L$  is the area of the CCD sensor,  $N$  is the number of pixels in one dimension, and  $\Delta x, \Delta y$  denote the sampling intervals or pixel size  $\Delta x = \Delta y = L/N$ .

Traditionally, in analog holography the reconstruction is performed by illuminating a holographic film by the conjugate of the reference beam  $E_R^*$ , and the real image is obtained from the last term of Eq. (1):  $|E_R|^2 E_O^*$ . The first two terms on the right-hand side and the third term contribute to the zero-order and the virtual image, respectively. The digital reconstruction is generally performed by numerically propagating the field  $E_R^* h(x, y)$  by the recording distance,  $d$  or  $-d$ , to reconstruct either the real or virtual images.

The Fresnel transform is based on the Fresnel approximation to the Huygens–Fresnel diffraction integral, and under the paraxial approximation, i.e.,  $d^3 \gg (2\pi/\lambda)[(\xi - x)^2 + (\eta - y)^2]$ , the reconstruction of the DH can be approximated by the Fresnel transformation as [23]

$$\Gamma(\xi, \eta) = z(\xi, \eta) F_{x,y} [h(x, y) E_R^*(x, y) w(x, y)]|_{k_x = \frac{2\pi\xi}{\lambda d}, k_y = \frac{2\pi\eta}{\lambda d}}, \quad (3a)$$

$$w(x, y) = \exp\left[-j\frac{\pi}{\lambda d}(x^2 + y^2)\right], \quad (3b)$$

$$z(\xi, \eta) = A \exp\left[-j\frac{\pi}{\lambda d}(\xi^2 + \eta^2)\right], \quad (3c)$$

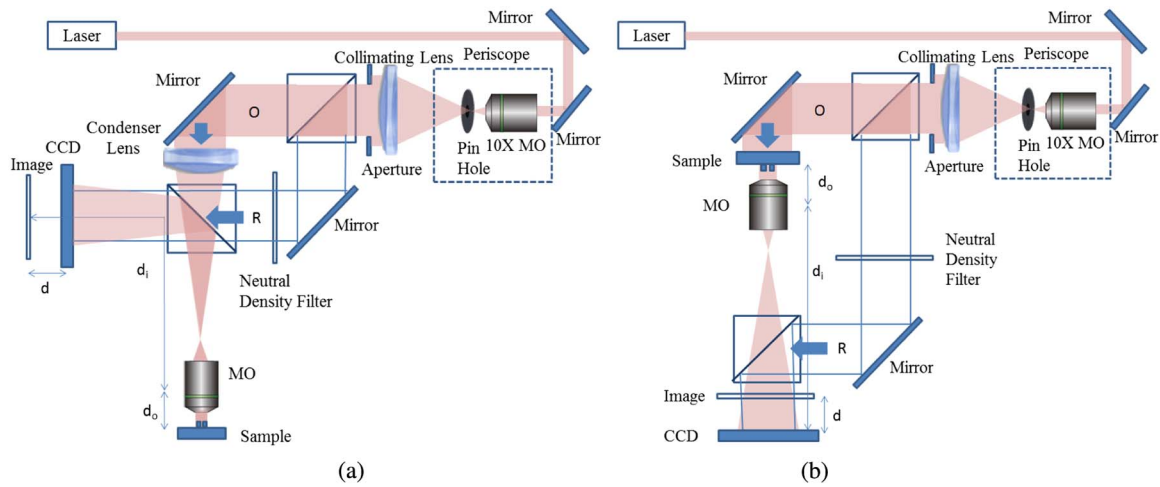


**Fig. 1.** SW/MW-DHM (a) reflective setup and (b) transmissive setup.

where  $A = \frac{j}{\lambda d} \exp(-\frac{j2\pi d}{\lambda})$ , and  $F_{x,y}\{E(x,y)\} = \int_{-\infty}^{\infty} \int_{-\infty}^{\infty} E(x,y) \exp[j(k_x x + k_y y)] dx dy$  is the Fourier transform. The intensity is calculated by squaring the optical field, i.e.,  $I(\xi, \eta) = |\Gamma(\xi, \eta)|^2$ , and the phase is calculated using  $\varphi(\xi, \eta) = \arctan(\text{Im}[\Gamma(\xi, \eta)] / \text{Re}[\Gamma(\xi, \eta)])$ . Note that 2D unwrapping algorithms need to be applied if  $\varphi(\xi, \eta)$  exceeds  $2\pi$ .

The reconstructed image resolution in  $\xi, \eta$  coordinates is given by

$$\Delta\xi = \lambda d / (N\Delta x), \quad \Delta\eta = \lambda d / (N\Delta y). \quad (4)$$

The image resolution given by Eq. (4) is considered to be “naturally scaled,” such that the value of  $\Delta\xi$  is automatically equal to the physical resolution limit imposed by the CCD sampled signal bandwidth. The angle between the reference wave and the object wave must not exceed the maximum angle which is  $\theta \leq \theta_{\max} = \arcsin(\frac{\lambda}{2\Delta x})$ , where  $\lambda$  is the wavelength, and  $\Delta x$  is the pixel size.

DHM is usually applied to determine 3D shapes of small objects, with height excursions of the order of microns (or phase excursions of the order of a few radians). Since small objects are involved, a MO of focal length  $f_o$  is often used to zoom onto a small area of the object to enhance the transverse resolution. Holograms of microscopic objects recorded with DHM setups can be numerically reconstructed in amplitude and phase using the same Fresnel DH reconstruction techniques. The phase aberrations due to the MO and the tilt from the reference beam have to be corrected to obtain the topographic profile or the phase map of the object [25–30]. Figures 1(a) and 1(b) show a Michelson SW/MW-DHM in reflection and transmission configurations, respectively. In reflection mode, an extra condenser lens of focal length  $f_c$  is used.

As stated above, in DHM we introduce a MO to increase the spatial resolution which was computed according to Eq. (4). Due to the magnification “ $M$ ” introduced by the MO, the pixel size in the image plane,  $\Delta\xi_{\text{mag}}$  and  $\Delta\eta_{\text{mag}}$ , scales according to

$$\begin{aligned} \Delta\xi_{\text{mag}} &= \Delta\xi / M = \lambda d / (N\Delta x M), \\ \Delta\eta_{\text{mag}} &= \Delta\eta / M = \lambda d / (N\Delta y M), \end{aligned} \quad (5)$$

which is simply the magnification  $M = d_i / d_o$  predicted by geometric imaging. This is intuitively understood by realizing that the holographic recording is now simply a recording of the geometrically magnified virtual image located at distance  $d$ , as shown in Fig. 2. Thus, the pixel resolution is automatically scaled accordingly. We can enhance the transverse resolution to be approximately equal to the diffraction limit of the MO, which is  $0.61\lambda/\text{NA}$ , where NA is the numerical aperture of the MO.

The reconstruction algorithm for traditional DHM systems is similar to Eq. (3a) [15,19,23]:

$$\begin{aligned} \Gamma(\xi, \eta) &= \exp\left[\frac{-j\pi}{\lambda D}(\xi^2 + \eta^2)\right]_{\text{Quadratic Phase due to MO}} \times z(\xi, \eta) \\ &\times F_{x,y}\{E_R^*(x,y)b(x,y)w(x,y)\}_{k_x=\frac{2\pi\xi}{\lambda d}, k_y=\frac{2\pi\eta}{\lambda d}}, \end{aligned} \quad (6)$$

where  $E_R^*(x,y) = A_R \exp[-j(k_{x0}x + k_{y0}y)]$  is the reconstructing reference wave, with  $A_R$  as the reference wave amplitude and  $k_{x0}, k_{y0} = k_0 \sin \theta_{x,y}$  as the transverse components of the propagation vector of the reference beam which can be found iteratively;  $\frac{1}{D} = \frac{1}{d_i}(1 + \frac{d_o}{d_i})$  is a parameter that must be computed to compensate for the wavefront curvature, and the focal

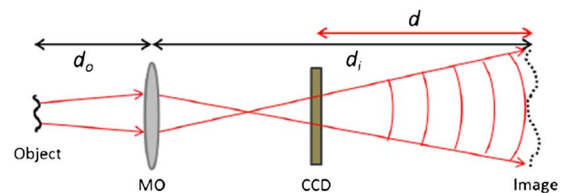


**Fig. 2.** Generalized holographic recording geometry using a lens. The image location is governed by geometric optics and may be on either side of the lens.



length of the MO is  $\frac{1}{f_o} = \frac{1}{d_i} + \frac{1}{d_o}$ . Equation (6) can be written in discretized form as

$$\Gamma(m, n) = A \exp \left[ \frac{-j\pi}{\lambda(d+D)} (m^2 \Delta \xi^2 + n^2 \Delta \eta^2) \right] \times F_{k,l} \{ E_R^*(k, l) h(k, l) w(k, l) \}_{m,n}, \quad (7)$$

where  $k, l, m, n$  are integers ( $-\frac{N}{2} \leq k, l, m, n \leq \frac{N}{2} + 1$ ),  $w(k, l) = \exp[-j\frac{\pi}{\lambda d} (k^2 \Delta x^2 + l^2 \Delta y^2)]$ , and  $E_R^*(k, l) = A_R \exp[-j(k_{x0} k \Delta x + k_{y0} l \Delta y)]$ . Since  $E_R^*$  is inside the Fourier transform integral, changing  $k_x, k_y$  introduces translation of the reconstructed image.  $E_R^*$  can be replaced by another  $E_R'$  outside the integral and Eq. (7) becomes [30]

$$\Gamma(m, n) = A \exp \left[ \frac{-j\pi}{\lambda(d+D)} (m^2 \Delta \xi^2 + n^2 \Delta \eta^2) \right] \times E_R'(m, n) \times F_{k,l} \{ h(k, l) w(k, l) \}_{m,n}, \quad (8)$$

where  $E_R'(m, n) = A_R \exp[-j(k_{x0} m \Delta \xi + k_{y0} n \Delta \eta)] \exp[j\frac{d}{2k_0} (k_{x0}^2 + k_{y0}^2)]$ .

In order to reconstruct the phase of the object accurately, the three parameters  $k_{x0}, k_{y0}$ , and  $D$  need to be adjusted simultaneously, with great accuracy, to avoid  $2\pi$  ambiguity due to the phases of the reference and MO, which obscure the true phase of the object.

For a reflective object on a reflective surface, the height profile on the sample surface is simply proportional to the reconstructed phase distribution  $\phi(m, n)$  through

$$h_z(m, n) = \frac{\lambda}{4\pi} \phi(m, n). \quad (9a)$$

For a transmissive phase object on a reflective surface, its thickness can be calculated as

$$h_z(m, n) = \frac{\lambda}{4\pi} \frac{\phi(m, n)}{\Delta n}, \quad (9b)$$

where  $\Delta n$  is the difference of the index of refraction between the transparent object material and the surrounding medium (e.g., air).

For a transmissive phase object on/transmissive surface/s, the phase change (optical thickness) can be calculated as

$$h_z(m, n) = \frac{\lambda}{2\pi} \frac{\phi(m, n)}{\Delta n}. \quad (9c)$$

Numerical techniques as well as optical configurations are usually employed to compensate for both the parabolic phase curvature and the phase tilt. One manual technique discussed in Section 2.D is based on using a phase mask during reconstruction, which requires knowledge of the setup parameters [19]. Another automatic technique based on 2D polynomial phase fitting is discussed in Section 2.F [30].

## B. Telecentric DHM Configuration (SW-TDHM)

In conventional lens systems, the magnification changes with object position change, the image has distortion, perspective errors, image resolution loss along the field depth, and edge position uncertainty due to object border lighting geometry. However, a telecentric system, such as the one shown in Fig. 3, provides nearly constant magnification, virtually eliminates

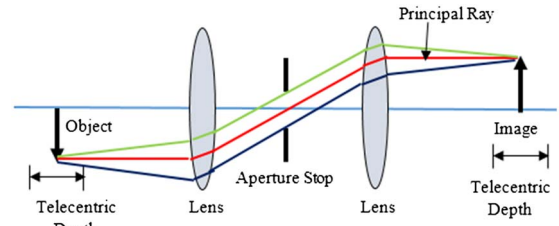


Fig. 3. Double telecentric system.

perspective angle error (e.g., objects with large depth will not appear tilted), and eliminates radial and tangential distortions [31–34]. In a bitemcentric system, both the entrance pupil and the exit pupil are located at infinity. Shifting either the image or object does not affect magnification, given that double telecentric systems are afocal.

As shown in Section 2.A, traditional DHM systems record a digital hologram using a MO. The object phase recovered from digital reconstruction using the Fresnel transform suffers from a parabolic phase factor introduced by the MO. Also, the phase tilt introduced by the reference beam results in linear fringes with high frequency that also obscure the real phase of the object. If the object parameters are unknown a two-step method is used, in which the hologram of a flat reference surface is initially recorded, and upon reconstruction it is subtracted from the hologram of the real object [35]. In this section, we adopt two telecentric configurations in reflection and transmission modes to remove optically, instead of numerically, the phase curvature due to the MO [31,32]. This telecentric setup can be used in either single-wavelength [32] or multiwavelength DHM configurations. It is worth noting that while operating in the nontelecentric mode, *a posteriori* numerical methods will not eliminate the phase aberration completely, as it depends on the sample location in the field of view [31]. Typical SW/MW-DHM setups using telecentric configurations in reflection and transmission modes are shown in Figs. 4(a) and 4(b), respectively.

In traditional DHM, the recorded wavefront on the CCD includes the interference of the reference wavefront and the total object wavefront. The total object phase consists of the defocused object phase on the image plane as well as the spherical (quadratic in paraxial approximation) phase due to propagation of the object wave from the image plane to the CCD. The object phase is expressed as [31]

$$\phi(x, y) = \frac{jk}{2R} (x^2 + y^2) + \phi_{ob}(x, y), \quad (10)$$

where  $R$  is the radius of curvature of the spherical curvature.

The telecentric system is used in an afocal configuration, where the back focal plane of the MO coincides with the front focal plane of the tube lens ( $f_o \equiv f_{TL}$ ), with the object placed at the front focal plane of the MO, resulting in the cancellation of the spherical phase curvature normally present in traditional DHM systems. Since  $d_f$  is the distance between the MO aperture stop and the TL, TDHM can be set with two different configurations: telecentric ( $d_f = f_{TL}$ ) and nontelecentric ( $d_f \neq f_{TL}$ ) [31]. The magnification of the telecentric DHM system is  $M = -f_{TL}/f_o$ . The reconstruction process can be done in a similar fashion to traditional DHM system by using the Fresnel transform:

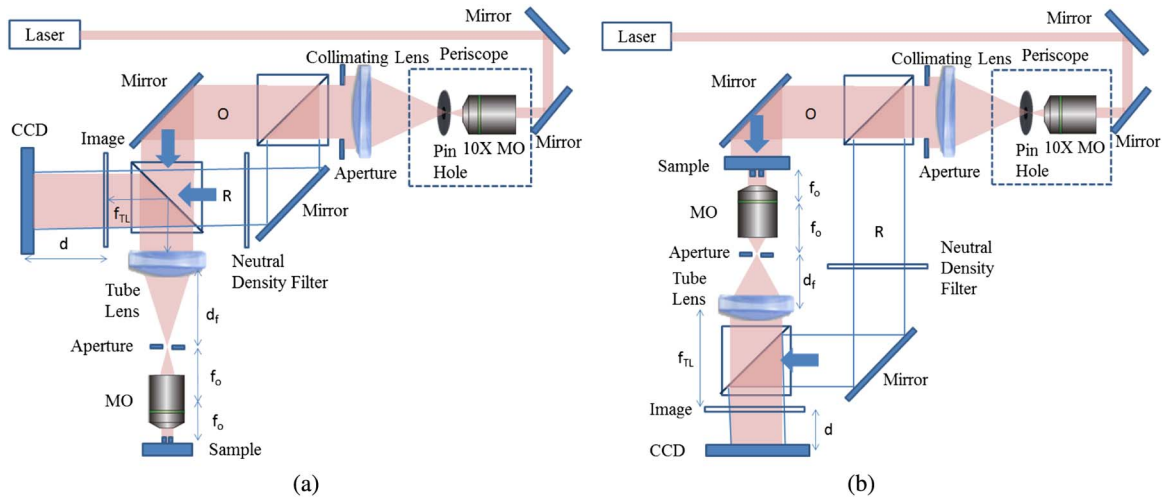


**Fig. 4.** Schematics of the SW/MW-TDHM setups: (a) reflection and (b) transmission configurations.

$$\Gamma(m, n) = A \exp \left[ \frac{-j\pi}{\lambda(d+C)} (m^2 \Delta \xi^2 + n^2 \Delta \eta^2) \right] \times F_{k,l} \{ E_R^*(k, l) b(k, l) w(k, l) \}_{m,n}, \quad (11a)$$

or from Eq. (8) we get

$$\Gamma(m, n) = A \exp \left[ \frac{-j\pi}{\lambda(d+C)} (m^2 \Delta \xi^2 + n^2 \Delta \eta^2) \right] E'_R(m, n) \times F_{k,l} \{ b(k, l) w(k, l) \}_{m,n}, \quad (11b)$$

where  $d$  is the reconstruction distance,  $A = -\frac{j}{\lambda d} \exp(\frac{i2\pi d}{\lambda})$ , and  $C = \frac{f_{TL}^2}{f_{TL} - d_f}$ . Hence, in the telecentric arrangement, the spherical phase is mostly eliminated, and  $k_{x0}$ ,  $k_{y0}$  need to be adjusted. In the case of minor defocusing,  $C \neq 0$ , a small residual spherical phase remains and can be easily compensated for by employing a 2D polynomial model. Details are in Sections 2.D and 2.F.

### C. Eliminating Zero-Order Diffraction and the Virtual Image Using Spatial Filtering

In off-axis DHM, there exists an angle  $\theta_{x,y} \leq \theta_{\max}$  between the reference beam  $E_R$  and the object beam  $E_O$  while interfering on the CCD plane and hence, from Eq. (6),  $E_R$  can be written as  $E_R = \exp(-jk_0(\sin \theta_x + \sin \theta_y))$ . This off-axis configuration leads to a translation of the spectrum of both the real and virtual images by  $\pm k_0 \sin \theta_{x,y}$  with respect to the zero order, which is located at the center in the Fourier domain. Thus,  $E_R$  has to be eliminated from inside the Fourier transform. For a certain region of interest (ROI), the real image can be spatially cropped and shifted to the center without affecting the quality of the reconstructed image. This operation can also be done optically by using a  $4f$  system and a notch-pass filter located at Fourier plane of the first lens. However, it is not easy to build up an optical notch-pass filter that can be translated spatially because the spectra of the virtual and real images change based on the angle of the reference beam. On the other hand, a digital binary notch-pass filter is a good choice to filter out the unwanted spectrum. It is worth mentioning that an automatic method to perform ROI centering based on applying a fitting procedure on the flat area

of the initial phase in the hologram plane is also possible [27]. This automatic method has limitations if the hologram does not contain enough background space or it is, for some other reason, hard to pick data for the fitting procedure.

Figure 5 shows the process for eliminating the zero-order and the virtual image spectrum using a numerically defined binary mask. Figure 5(a) shows the original transmission hologram, which is the interference between the reference and object beam while the object is not mounted (in reflection mounting, a mirror instead of the object will produce same result), Fig. 5(b) shows the reconstructed intensity image, and Fig. 5(c) shows the Fourier transform of the hologram, where the regions corresponding to the zero-order, virtual, and real images are clearly marked. Figure 5(d) shows the cropped spectrum and the reconstructed intensity around the real image. Figure 5(e) shows the filtered spectrum and reconstructed intensity of the ROI around the location of the real image shifted to the center of the observation plane. As a result of this process, the contrast of the reconstructed real image is enhanced because the notch-pass filter eliminates the high-intensity low frequency that overlaps with the real image. The process of shifting the real image's spectrum to the center can be achieved automatically by locating the position of the maximum amplitude in the ROI around the real image's spectrum. In telecentric systems, locating the maximum pixel intensity is relatively easy since the maximum is sharp. However, in nontelecentric systems, the spectrum of the real image is spread over a broader area due to the curvature of the MO and it is difficult to locate the position of the spectrum maximum accurately [27]. One easy way is to create a rectangular notch-pass filter covering the entire real image's spectrum and translating it in such a way that the center of real image's spectrum is exactly at the center of entire spectrum.

### D. Digital Correction of Phase Aberrations Using a Manual Phase Mask

Manual aberration compensation can be performed using a phase mask  $\Psi$  to cancel the effects of the quadratic phase due to the MO. The phase mask that compensates for the

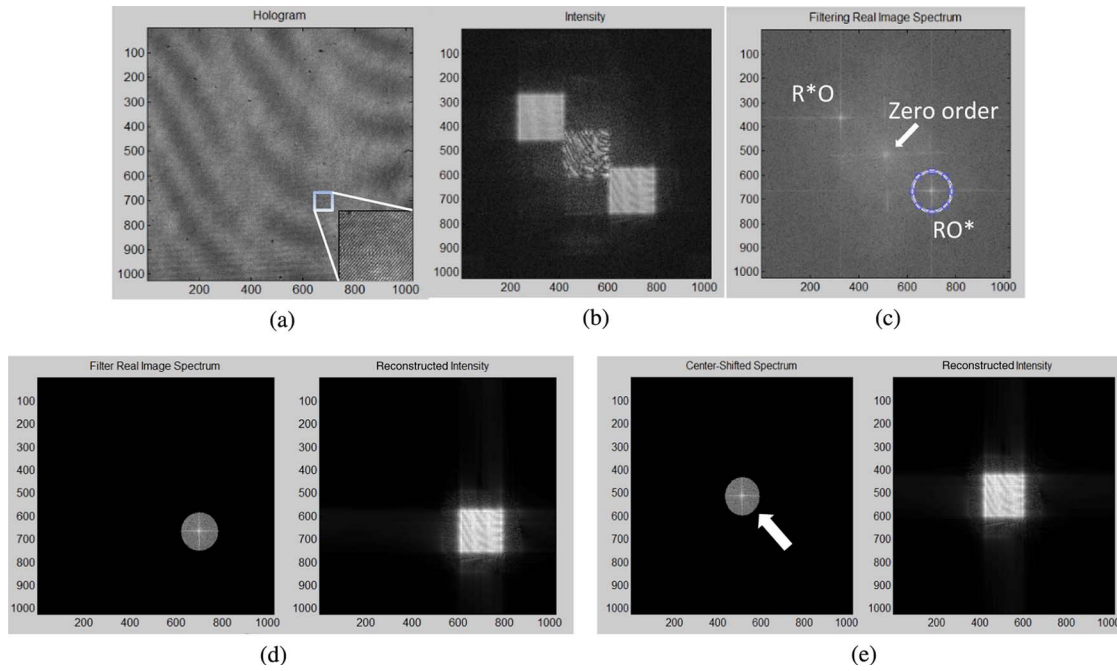


**Fig. 5.** (a) Hologram of the background while the object is not mounted, (b) reconstructed intensity, (c) Fourier transform of the hologram, (d) eliminated zero-order and virtual image spectrum (left) and reconstructed intensity (right) after filtering, and (e) center-shifted spectrum and reconstructed intensity from (d).

MO curvature in the cases of nontelecentric and partially telecentric setups can be written as [19]

$$\Psi(m, n) = \exp \left[ \frac{j\pi}{\lambda D} (m^2 \Delta \xi^2 + n^2 \Delta \eta^2) \right], \quad (12a)$$

$$\Psi(m, n) = \exp \left[ \frac{j\pi}{\lambda C} (m^2 \Delta \xi^2 + n^2 \Delta \eta^2) \right], \quad (12b)$$

where  $D$  and  $C$  parameters are defined in Eqs. (6), (11a), and (11b), respectively.

The phase reconstructed from traditional DHM always suffers from a parabolic phase factor introduced by the MO. By introducing the term  $\Psi(m, n)$  into Eqs. (8) and (11b), we get

$$\Gamma(m, n) = A\Psi(m, n) \exp \left[ \frac{-j\pi}{\lambda(d+D)} (m^2 \Delta \xi^2 + n^2 \Delta \eta^2) \right] \times E'_R(m, n) \times F_{k,l} \{ h(k, l) w(k, l) \}_{m,n} \quad (13a)$$

$$\Gamma(m, n) = A\Psi(m, n) \exp \left[ \frac{-j\pi}{\lambda(d+C)} (m^2 \Delta \xi^2 + n^2 \Delta \eta^2) \right] \times E'_R(m, n) \times F_{k,l} \{ h(k, l) w(k, l) \}_{m,n} \quad (13b)$$

In traditional SW-DHM, the reconstructed phase has a paraboloid phase term and other phase aberrations. With known reconstruction parameters, the system must be tediously calibrated first by accurately adjusting the three parameters: parabolic phase  $D$  and reference angles  $k_{x0}$  and  $k_{y0}$ . Failing to do that, the phase distribution will be obscured. By using the telecentric setup shown in Figs. 4(a) and 4(b), the  $C$  parameter is zero. Hence, when using a telecentric configuration, the

paraboloid phase is cancelled optically. The DHM system can also outperform the traditional DHM system shown in Fig. 1 even if it is operated in a partially telecentric configuration ( $C \approx \infty$ , or  $f_{TL} \approx d_f$ ). Hence, an extra step in the process is eliminated and only  $k_{x0}$  and  $k_{y0}$  need to be adjusted. Even with a telecentric arrangement, higher order phase aberrations caused by other optical components, chromatic aberrations, and misalignments still exist. Digital correction for phase aberrations is necessary because it is more convenient than optical correction. Another way to perform aberration compensation is to measure the background phase without the sample, take another measurement with the sample, and subtract the background phase [29]. However, this step requires a perfect mechanical replacement. A more robust technique is to perform automatic aberration cancellation by approximating the residual phase front due to aberration using 2D polynomial models to create a phase mask  $\Psi(m, n)$  that can cancel the phase aberration. Details are given in Section 2.F [30].

### E. Digital Correction to Minimize Intensity and Phase Fluctuations Using Apodization

The numerical reconstruction method shown in Eqs. (13a) and (13b) involves Fresnel diffraction of a hologram limited to a finite aperture. The edges of the aperture cause fluctuations in the reconstructed intensity and phase, which apodization may be used to minimize [25]. A cubic spline is employed to digitally generate the apodization of the aperture of the holograms recorded by a CCD camera. The apodized window shown in Fig. 6(a) is created by the function  $T(m, n) = T(m) \times T(n)$ , where  $T(m)$  and  $T(n)$  are two one-dimensional functions in the  $x$  and  $y$  directions at the



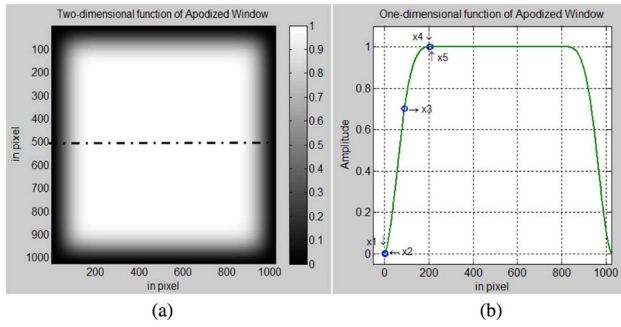


**Fig. 6.** Digitally apodized window with  $T(m) = T(1024, 0.6, 2.5e^{-3}, 90, 0.69)$ . (a) Apodized window  $T(m, n)$ , where the edge of the aperture follows a cubic spline interpolation, and (b) slice plot of the apodized window shown in (a) [25].

observation plane.  $T(m) = T(N, p, d_0, x_3, y_3)$  is the function shown in Fig 6(b), where  $N$  is the pixel size of the CCD,  $p$  is the ratio:  $\frac{[\text{Num. of pixels of } T(m_i)=1]}{N}$ , and  $d_0$  is the first derivative of  $T'(m)|_{m=x_1}$ . The curve  $T(m)$  is formed by using cubic spline interpolation through five points with  $x = [x_1, x_2, x_3, x_4, x_5] = [1, 2, x_3, x_5 - 1, x_5]$  in pixels corresponding to  $y = [y_1, y_2, y_3, y_4, y_5] = [0, d_0, y_3, 1, 1]$  in amplitude, and  $x_5 = \text{round}(N - Np)/2$  [25].

The effects of apodization can be analyzed in Fig. 7. Figure 7(a) shows a simulated recorded hologram before and after apodization, where  $T(m) = T(1024, 0.60, 2.5e^{-3}, 90, 0.7)$ . The blue curves in Fig. 7(d) show the cross section of the reconstructed amplitude and phase from Fig. 7(b) without apodization in blue, while the red curves show the cross section of the reconstructed amplitude and phase from Fig. 7(c) after apodization. The wavefront reconstructed using apodization is not a perfect plane wave over the whole area; however, the oscillation is significantly reduced. The center area is approximately constant and still covers enough area for sample objects to be investigated. Outside of this area, large fluctuations still exist.

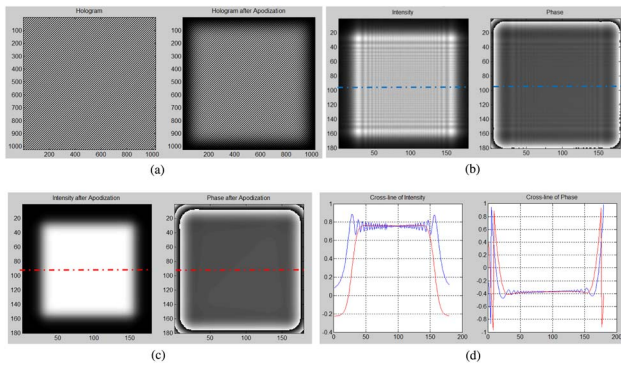


**Fig. 7.** Simulation of a digital hologram with  $T(m) = T(1024, 0.6, 2.5e^{-3}, 90, 0.7)$ . (a) Simulated hologram (interference from two plane waves) before and after apodization, (b) reconstructed intensity and phase using Eqs. (11a) and (11b), (c) reconstructed intensity and reconstructed phase with apodization, and (d) cross section of the reconstructed amplitude and the reconstructed phase before (blue) and after (red) apodization.

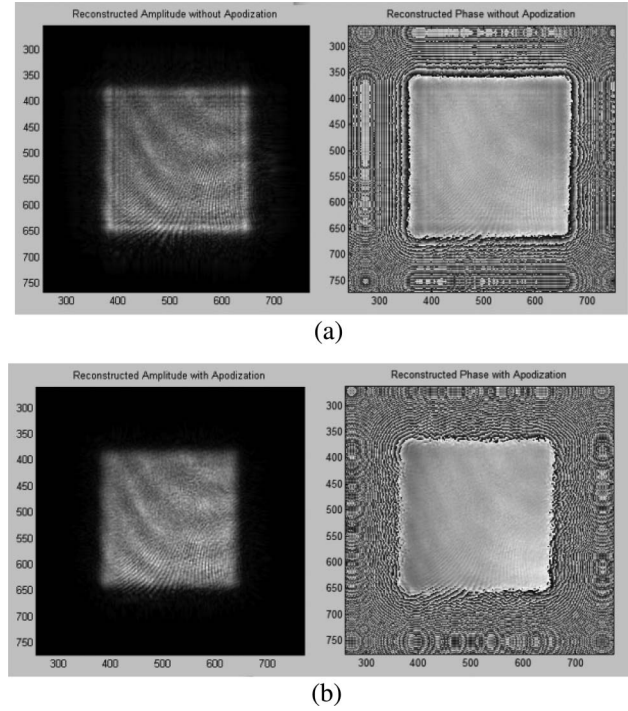


**Fig. 8.** Reconstructed intensities and phases with (a) apodization and (b) without apodization in the reflection mode with a mirror as the sample object.

Figure 8 shows the reconstructed intensity and phase using the setup in Fig. 4(a) in reflection mode, using apodization, where the sample object is a mirror. As a result, the oscillations of the reconstructed intensity and phase distributions are significantly reduced. However, the center area is not as flat as predicted by the simulation due to the various aberrations of optical components and/or slight misalignments. Also, we can see low-frequency fringes in the center area which are due to interference from the double reflection within the cover glass on the CCD sensor.

## F. Digital Correction of Phase Aberrations Using 2D Polynomial Models

In this section and for each DHM configuration discussed before, we employ 2D polynomial models to perform 2D surface fitting to compensate digitally for chromatic aberration (in the multiwavelength case) and for higher order phase aberrations. Table 1 shows the Zernike polynomials in Cartesian coordinates that are used to model aberrations and create the phase mask  $\psi'(m, n)$  [30]. In all the experiments, we used 21 polynomials to mimic the phase aberration. The algorithm for aberration compensation using 2D polynomial models is as follows:

- Define the mathematical model for the 2D surface fitting  $\psi'(m, n)$ , which consists of either 2D regular or Zernike polynomials.
- Choose the maximum order for the 2D polynomials to model the 2D phase aberration. In all experiments below,  $K = 21$  polynomials up to the  $L = 5$ th order in  $x$  and  $y$ , were chosen.
- Calculate the polynomial coefficients  $p_{lk}$  or  $a_k$  and solve the linear system of equations (see below).



Table 1. Zernike Standard Coefficients Using Zemax Classification

Polynomial Coefficients	Cartesian Form- $Z_k$	Type
$a_0$	1	Piston
$a_1$	$\sqrt{4}x$	Tilt x
$a_2$	$\sqrt{4}y$	Tilt y
$a_3$	$\sqrt{3}(2x^2 + 2y^2 - 1)$	Power
$a_4$	$\sqrt{6}(2xy)$	Astig y
$a_5$	$\sqrt{6}(x^2 - y^2)$	Astig y
$a_6$	$\sqrt{8}(3x^2y + 3y^2 - 2y)$	Coma y
$a_7$	$\sqrt{8}(3x^3 + 3xy^2 - 2x)$	Coma x
$a_8$	$\sqrt{8}(3x^3y - y^3)$	Trefoil y
$a_9$	$\sqrt{8}(x^3 - 3xy^2)$	Trefoil x
$a_{10}$	$\sqrt{5}(6x^4 + 12x^2y^2 + 6y^4 - 6x^2 - 6y^2 + 1)$	Pri Spherical
$a_{11}$	$\sqrt{10}(4x^4 - 3x^2 + 3y^2 - 4y^4)$	2 <sup>ary</sup> Astig x
$a_{12}$	$\sqrt{10}(8x^3y - 8xy^3 - 6xy)$	2 <sup>ary</sup> Astig y
$a_{13}$	$\sqrt{10}(x^4 - 6x^2y^2 + y^4)$	Tetrafoil x
$a_{14}$	$\sqrt{10}(4x^3y - 4xy^3)$	Tetrafoil y
$a_{15}$	$\sqrt{12}(10x^5 + 20x^3y^2 + 10xy^4 + 12x^3 - 12xy^2 + 3x)$	2 <sup>ary</sup> Comma x
$a_{16}$	$\sqrt{12}(10x^4y + 20x^2y^3 + 10y^5 + 12x^2y - 12y^3 + 3y)$	2 <sup>ary</sup> Comma y
$a_{17}$	$\sqrt{12}(5x^5 - 10x^3y^2 - 15xy^4 - 4x^3 + 12xy^2)$	2 <sup>ary</sup> Tetrafoil x
$a_{18}$	$\sqrt{12}(15x^4y + 10x^2y^3 - 5y^5 - 12x^2y + 4y^3)$	2 <sup>ary</sup> Tetrafoil y
$a_{19}$	$\sqrt{12}(x^5 - 10x^3y^2 + 5xy^4)$	Pentafoil x
$a_{20}$	$\sqrt{12}(5x^4y - 10x^2y^3 + y^5)$	Pentafoil y
$a_{21}$	$\sqrt{7}(20x^6 + 60x^4y^2 + 60x^2y^4 + 20y^6 - 30x^4 - 60x^2y^2 - 30y^4 + 12x^2 + 12y^2 - 1)$	2 <sup>ary</sup> Spherical
$a_{22}$	$\sqrt{14}(30x^5y + 60x^3y^3 + 30xy^5 - 40x^3y - 40xy^3 + 12xy)$	3 <sup>ary</sup> Astig x
$a_{23}$	$\sqrt{14}(15x^6 + 15x^4y^2 - 20x^4 + 6x^2 - 15x^2y^4 - 15y^6 + 20y^4 - 6y^2)$	3 <sup>ary</sup> Astig y

iv. Create the mask  $\psi'(m, n) = \exp(-j \sum_{k=0}^K a_k Z_k)$  or  $\psi'(m, n) = \exp(-j \sum_{l=0}^L \sum_{k=0}^{L-l} p_{lk} x^l y^k)$ .

v. Reconstruct the hologram intensity and phase using Eqs. (13a) and (13b).

In order to cancel the phase aberration, the phase data were chosen at locations with a known, flat phase, similar to the mirror. Based on the chosen data, 2D surface fitting generates a phase mask based on the background information. Curve fitting was done in MATLAB after converting the 2D phase data to a 1D vector. The 2D polynomial used is of fifth order with 21 coefficients where  $x$  and  $y$  represent pixel coordinates. The regular polynomial model has the following form:

$$S(x, y) = \sum_{l=0}^5 \sum_{k=0}^{5-l} p_{lk} x^l y^k, \quad l + k \leq 5. \quad (14)$$

Let the arrays  $\mathbf{P} = [p_{00} \ p_{10} \dots p_{50} \dots p_{05} \dots p_{55}]$  and  $\mathbf{A} = [a_0 \ a_1 \dots a_{10} \dots a_{20}]$  hold the polynomial model's coefficients and the Zernike model's coefficients, respectively, where  $l, k$  represent the polynomial order in  $x$  and  $y$ , respectively. The 21 coefficients of the  $\mathbf{P}$  polynomial are used to calculate the coefficients of the Zernike polynomial model, as shown in the following equation:

$$\mathbf{A} = \mathbf{z}_{l,k,p}^{-1} \cdot \mathbf{P}, \quad (15)$$

where  $\mathbf{z}_{l,k,p}$  is a matrix of size  $(p+1) \times (p+1)$  (since the number of coefficients of a 2 variable polynomial of maximum degree in  $x$  and  $y$  of 5 is  $\binom{2+5}{5} = \frac{(2+5)!}{5!2!} = 21 = p+1$ ).

The  $\mathbf{z}_{l,k,p}$  matrix consists of coefficients corresponding to each order of the Zernike polynomials

$$\begin{bmatrix} a_0 \\ a_1 \\ \vdots \\ a_{10} \\ \vdots \\ a_{20} \end{bmatrix} = \begin{bmatrix} z_{0,0,0} & z_{0,0,1} & \dots & z_{0,0,10} & \dots & z_{0,0,p-1} & z_{0,0,p} \\ z_{1,0,0} & z_{1,0,1} & \dots & z_{1,0,10} & \dots & z_{1,0,p-1} & z_{1,0,p} \\ \vdots & \vdots & \ddots & \vdots & \ddots & \vdots & \vdots \\ z_{4,0,0} & z_{4,0,1} & \dots & z_{4,0,10} & \dots & z_{4,0,p-1} & z_{4,0,p} \\ \vdots & \vdots & \ddots & \vdots & \ddots & \vdots & \vdots \\ z_{0,5,0} & z_{0,5,1} & \dots & z_{0,5,10} & \dots & z_{0,5,p-1} & z_{0,5,p} \end{bmatrix}_{p=20}^{-1} \cdot \begin{bmatrix} p_{00} \\ p_{10} \\ \vdots \\ p_{40} \\ \vdots \\ p_{05} \end{bmatrix}, \quad (16)$$

The Zernike polynomial model is used to construct the phase  $\psi'(m, n) = \exp(-j \sum_{k=0}^{20} a_k Z_k)$ , where  $\mathbf{Z}_k$  coefficients are expressed according to the Zemax classification and shown in Table 1. Figure 9 shows a phase measurement example of group 6 and group 7 of the USAF 1951 resolution test target using SW-DHM and applying 2D surface fitting to calculate

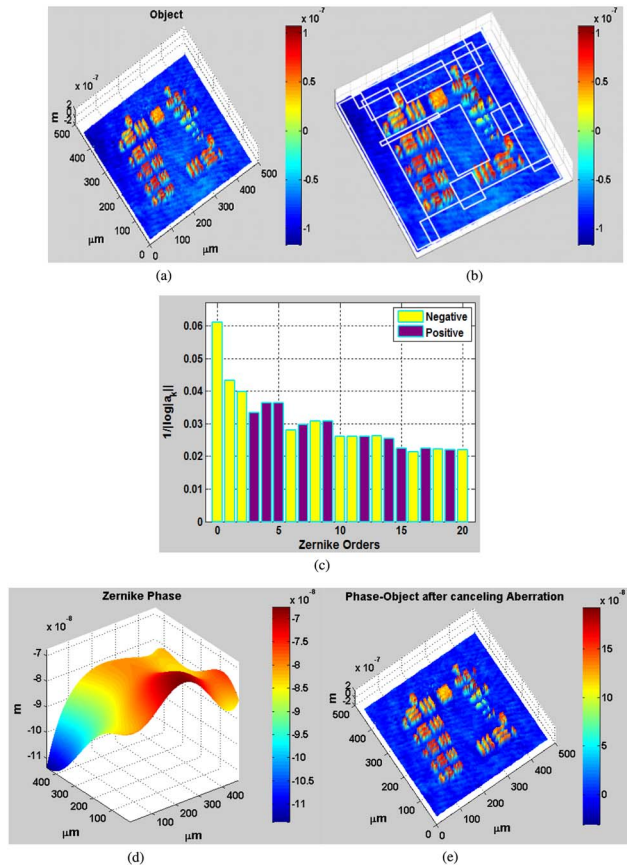


**Fig. 9.** 2D surface fitting to calculate the Zernike polynomial model: (a) reconstructed 2D height profile (in meters) of the object containing aberration, (b) same as (a) showing white rectangles where cropped areas are used in the 2D surface fitting process, (c) Zernike coefficients displayed as a  $1/|\log_{10}(|a_k|)|$  histogram, (d) phase generated from the Zernike model (converted to height), and (e) reconstructed 2D height profile (in meters) of the object after canceling phase aberrations.

the Zernike polynomial model. Figure 9(a) shows the reconstructed phase of the object containing aberration. Notice the phase aberration on the planar surface beneath the object features. In order to obtain a successful fitting process, the background is chosen by cropping areas of the surface where the object is known to be flat. Figure 9(b) shows the cropped areas as white rectangles that are used in the 2D surface fitting process. This process can be done automatically if the locations of the flat areas of the object are known *a priori*. Figure 9(c) shows the Zernike coefficients that are calculated using Eq. (16) and are displayed as  $1/|\log_{10}(|a_k|)|$ . Because of the large difference between the low-order coefficients and the high-order coefficients, the log function is used to reduce the range for better visualization. Moreover, the inverted log function ( $1/|\log|$ ) is used to ensure the coefficients that contribute to large aberrations appear larger. Figure 9(d) shows the phase generated from the Zernike model, and Fig. 9(e) shows the reconstructed phase of the object after canceling phase aberrations.

Figure 10(a) shows another example of a reconstructed object (made of four bars) phase (in radians) before aberration

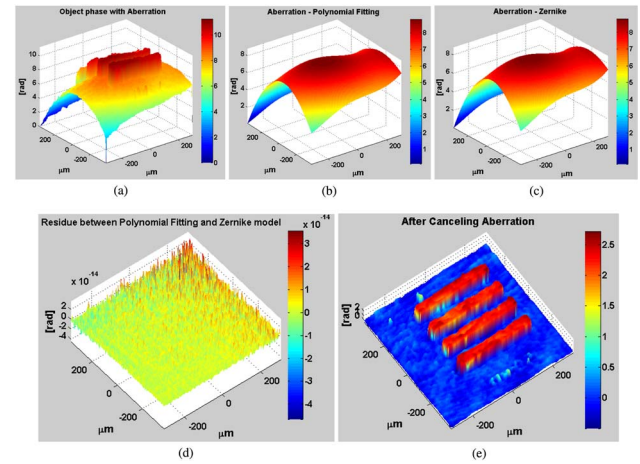


**Fig. 10.** (a) Reconstructed object phase before aberration cancellation, (b) aberration model using polynomial approximation from Eq. (14), (c) aberration model using the Zernike polynomial approximation from Eq. (16), (d) the difference between (b) and (c), and (e) reconstructed object phase after aberration cancellation.

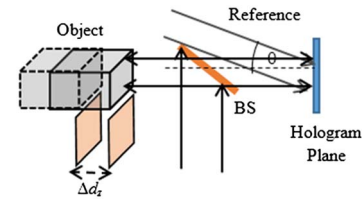


**Fig. 11.** Path difference of the light rays on their way from the source to the object and from the object to the hologram plane for different  $z$  distances.

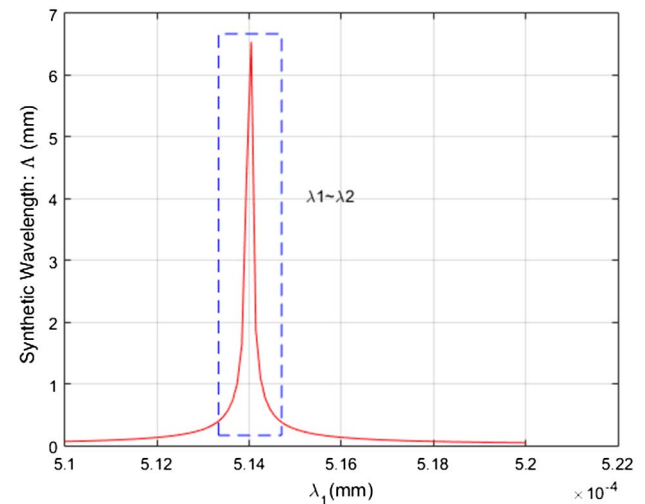


**Fig. 12.** MWDH extends the vertical measurement range without phase ambiguity. In this example,  $\lambda_2$  is approaching  $\lambda_1 = 514$  nm, resulting in a synthetic wavelength of several millimeters.

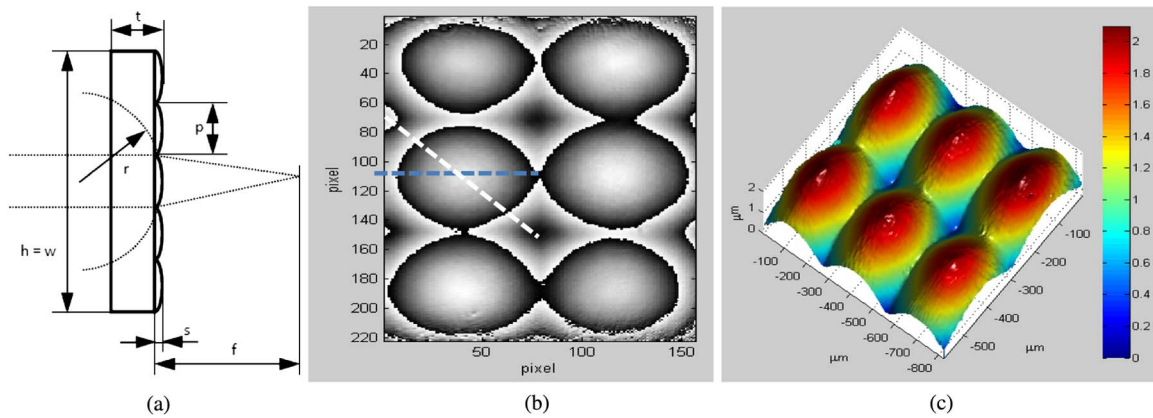


**Fig. 13.** (a) An illustration of the lens array dimensions looking from the side, (b) the reconstructed wrapped phase after automatic aberration cancellation, and (c) the 3D unwrapped reconstructed profile.

cancellation. Figures 10(b) and 10(c) show the aberration model using polynomial fitting and Zernike polynomial fitting, as defined in Eqs. (14) and (16), respectively. Figure 10(d) shows the difference between the two models. Notice that the maximum of the difference between the two techniques is less than  $4.5e-14$  rad, which verifies that both fitting techniques give the same result. Figure 10(e) shows the reconstructed object phase after aberration cancellation.

### 3. THEORETICAL STUDY OF TELECENTRIC AND NONTLECENTRIC MW-DHM

It is well known that a primary application of holographic interferometry is the generation of fringe patterns corresponding to contours of constant elevation with respect to a reference plane [21,23]. These contour fringes can be used to determine the shape of a macroscopic or microscopic three-dimensional object. There exist three main techniques to create holographic contour interferograms: (a) the two-illumination-point method, (b) the two-refractive-index technique, which is generally not practical because we must change the refractive index of the medium where the object is located, and (c) the multiwavelength method, which was adopted in this section [14,15]. For large height profiles (larger than several microns), measuring 2D topography using the single-wavelength holographic approach is not appropriate since phase unwrapping has limitations, especially for sharp-edge variations. As shown in Fig. 11, the axial displacement of an image recorded with wavelength  $\lambda_1$  and reconstructed with another wavelength  $\lambda_2$ , with respect to the image recorded and reconstructed with  $\lambda_2$ , is [21,23]

$$\Delta d_z = z \frac{|\lambda_1 - \lambda_2|}{\lambda_2}. \quad (17)$$

This means that the phase shift depends on the distance  $z$  between the object and the hologram plane. The height jump between two adjacent fringes in the reconstructed image is

$$\begin{aligned} \Delta H &= z(\Delta\phi = 2\pi(n+1)) - z(\Delta\phi = 2\pi n) \\ &= \frac{\lambda_1 \lambda_2}{2|\lambda_1 - \lambda_2|} = \frac{\Lambda}{2}, \end{aligned} \quad (18)$$

where  $\Lambda$  is known as the synthetic wavelength. For larger deformations along the  $z$  direction, the phase changes could be hundreds of multiples of  $2\pi$ . Such large fringe densities may lead to difficulty in determining the object phase using the single-wavelength technique. However, multiwavelength illumination encodes the object height in terms of  $2\pi$  multiples of the synthetic wavelength, which is generally much longer than either fundamental wavelength. This allows larger object deformations to be measured by multiwavelength illumination as if illuminated by the single-wavelength method, where the “single” wavelength is now given by the synthetic wavelength  $\Lambda$ . Typically, synthetic wavelengths can range from a few microns to tens of microns [14,34]. The topographic resolution is

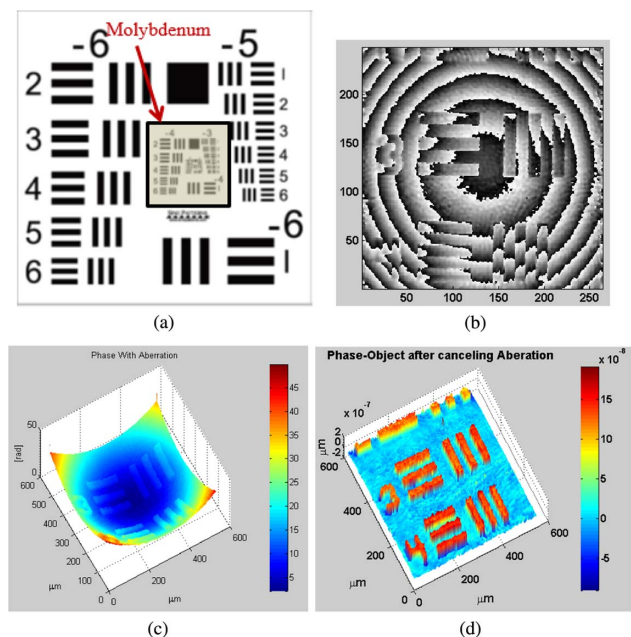


**Fig. 14.** 3D Profile reconstruction using a SW-DHM nontelecentric setup. (a) Group 4, elements 3 and 4 of a 1951 USAF resolution chart with a  $\sim 50$  nm reflective molybdenum film sputtered onto it. (b) Reconstructed wrapped phase, (c) reconstructed unwrapped phase (3D profile) with aberration, and (d) reconstructed phase (3D profile) after automatic aberration cancellation using Zernike polynomials.



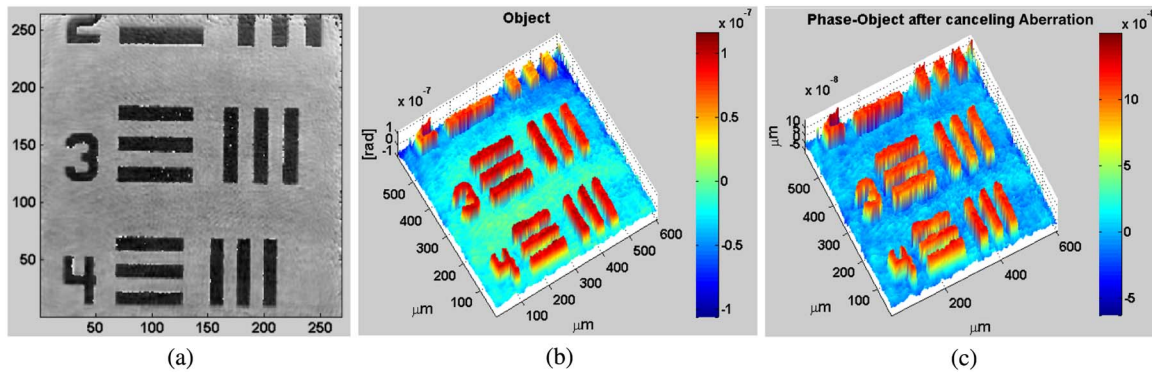


**Fig. 15.** 3D profile reconstruction, using SW-TDHM, of a USAF 1951 resolution target, group 4, elements 3 and 4 [see Fig. 14(a)]. (a) 2D reconstructed unwrapped phase with aberrations, (b) 3D profile with aberrations, and (c) 3D profile after automatic aberration cancellation.

typically of the order of  $1/100$  of  $\Lambda$ , and the vertical measurement range can reach several  $\Lambda$ s by employing phase unwrapping for heights larger than  $\Lambda$  [24]. However, much longer synthetic wavelengths may also be used to measure millimeter-scale features. Figure 12 shows the advantages of using MWDH to extend the vertical measurement range without phase ambiguity.

In multiwavelength DH, both holograms are reconstructed separately at the correct fundamental wavelengths,  $\lambda_1$  or  $\lambda_2$ . From the resulting reconstructed complex amplitudes  $\Gamma_{\lambda_1}(\xi, \eta)$  and  $\Gamma_{\lambda_2}(\xi, \eta)$ , the phases are calculated as

$$\phi_{\lambda_{1,2}}(m, n) = \arctan\left(\frac{\text{Im}\Psi_{\lambda_{1,2}}(m, n)}{\text{Re}\Psi_{\lambda_{1,2}}(m, n)}\right). \quad (19)$$

The synthetic wavelength phase image is now calculated directly by pixelwise subtraction of the fundamental wavelength hologram phases

$$\delta\phi(m, n) = \begin{cases} \phi_{\lambda_1} - \phi_{\lambda_2}, & \text{if } \phi_{\lambda_1} > \phi_{\lambda_2}, \\ \phi_{\lambda_1} - \phi_{\lambda_2} + 2\pi, & \text{if } \phi_{\lambda_1} < \phi_{\lambda_2}. \end{cases} \quad (20)$$

This phase map is equivalent to the phase distribution of a hologram recorded with the *synthetic wavelength*

$$\Lambda = \frac{\lambda_1 \lambda_2}{|\lambda_1 - \lambda_2|}. \quad (21)$$

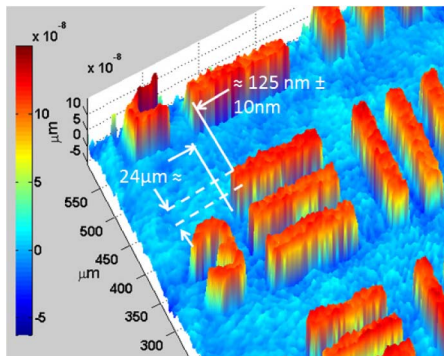
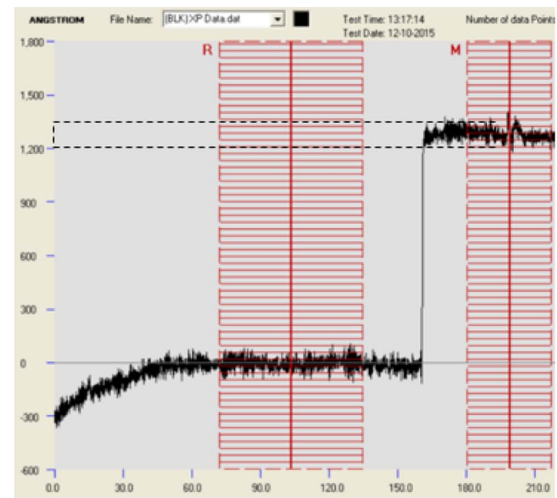
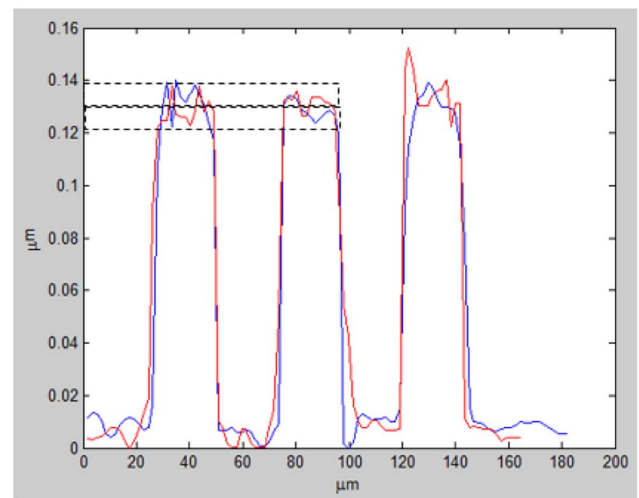


**Fig. 16.** Vertical height and transverse width of the USAF target at group 4 element 3.



(a)



(b)

**Fig. 17.** Measurements of the USAF 1951 target at group 4 element 3. (a) Profilometry measurement for one-step height (the vertical axis is in angstroms), and (b) comparison between the measured height in nontelecentric (red) and telecentric (blue) setups, respectively.



At normal incidence, a  $2\pi$  phase jump corresponds to a height step of  $\Lambda/2$ , and the change in longitudinal distance or height  $\Delta z$  is given by [21,23]

$$\Delta z = \left( \frac{\Delta\phi}{2\pi} \right) \frac{\Lambda}{2} = \left( \frac{\Delta\phi}{2\pi} \right) \left( \frac{\lambda_1 \lambda_2}{2|\lambda_1 - \lambda_2|} \right) = \left( \frac{\Delta\phi}{2\pi} \right) \Delta H. \quad (22)$$

Note that the transverse resolution is the same as in DH, namely,  $\Delta\xi = \lambda d / N \Delta x$  is the reconstructed pixel size. Similar to SWDH, the MWDH setup can be constructed using the Mach-Zehnder or Michelson configuration. True height measurements in Mach-Zehnder and Michelson configurations are

$$\Delta\lambda_{\text{True, Mach-Zehnder}} = \left( \frac{\Delta\phi}{2\pi} \right) \frac{\Lambda}{2} \cos \theta, \quad (23a)$$

$$\Delta\lambda_{\text{True, Michelson}} \approx \left( \frac{\Delta\phi}{2\pi} \right) \frac{\Lambda}{2}, \quad (23b)$$

respectively. Note that in telecentric systems, achromatic lenses can be employed to minimize achromatic aberration due to the use of multiwavelength illumination.

One important detail that must be considered when applying the two-wavelength technique is pixel matching. Recall from Eq. (4) that the pixel resolution  $\Delta\xi$  of each hologram is dependent upon the fundamental recording wavelength ( $\lambda_1$  or  $\lambda_2$ ). In order for the reconstruction to be successful, the subtraction described by Eq. (20) must be performed on a pixel-by-pixel basis, in which the pixel sizes match between each hologram (i.e.,  $\Delta\xi_1 = \Delta\xi_2$ ). This can be accomplished by zero-padding the holograms to alter the numerical resolution

according to the following procedure. One hologram is zero-padded prior to reconstruction such that its value of  $\Delta\xi$  matches that of the second hologram. The second hologram is then either zero-padded after reconstruction or the first hologram (which is now larger) is cropped, such that the total sizes of each image are again equal. If it is assumed that  $\lambda_1 > \lambda_2$ , then the degree of padding applied to both the  $\lambda_1$  hologram prereconstruction and the  $\lambda_2$  hologram postreconstruction is

$$\text{pad size} = \text{round} \left[ \frac{N}{2} \left( \frac{\lambda_1}{\lambda_2} - 1 \right) \right], \quad (24)$$

where pad size is the number of zero elements to be added symmetrically to each edge of the hologram matrix, rounded to the nearest integer value.

## 4. EXPERIMENTAL RESULTS

### A. SW-DHM Using a Nontelecentric Setup

The first experiment aims at characterizing the 3D profile of a  $b:10 \text{ mm} \times w:10 \text{ mm} \times t:1.2 \text{ mm}$ ,  $p = 300 \text{ }\mu\text{m}$  pitch, square lattice, plano-convex parabolic microlens array of focal length  $f = 18.6 \text{ mm}$  acting as phase object using SW-DHM in the nontelecentric setup shown in Fig. 1(b). The microlens radius of curvature is  $r = 8.6 \text{ mm}$  and the maximum height variation from one side to the other is  $s = 1.31 \text{ }\mu\text{m}$  (see the blue dashed line), while the maximum height variation diagonally is  $s = 2.61 \text{ }\mu\text{m}$  (see the white dashed line) shown in Fig. 13(b). The surface heights are different because of the square lattice. Figure 13(a) shows the dimensions of the lens array. Figure 13(b) shows the reconstructed phase after using automatic aberration cancellation, and Fig. 13(c) shows the 3D reconstructed profile after phase unwrapping.

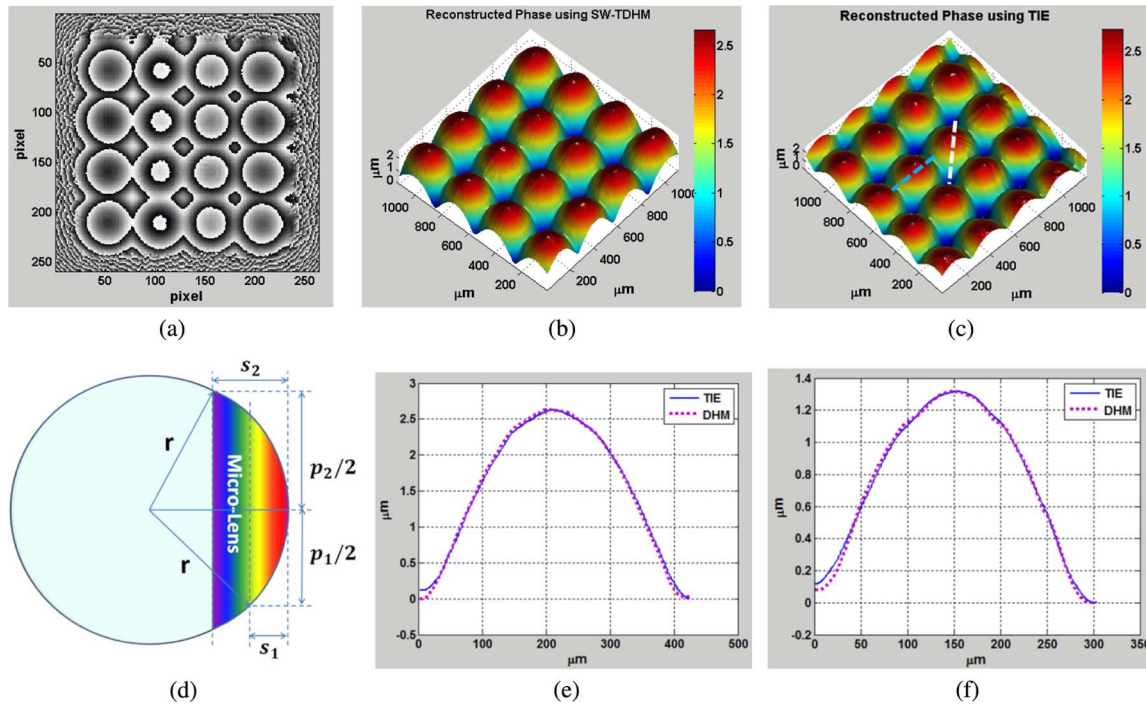


**Fig. 18.** (a) Reconstructed wrapped phase, (b) 3D unwrapped reconstructed profile after automatic aberration cancellation, and (c) 3D profile obtained using the TIE. (d) Geometric illustration of the sample dimensions. Comparison between the TIE and SW-DHM techniques along (e) the dashed white line and (f) the dashed blue line.

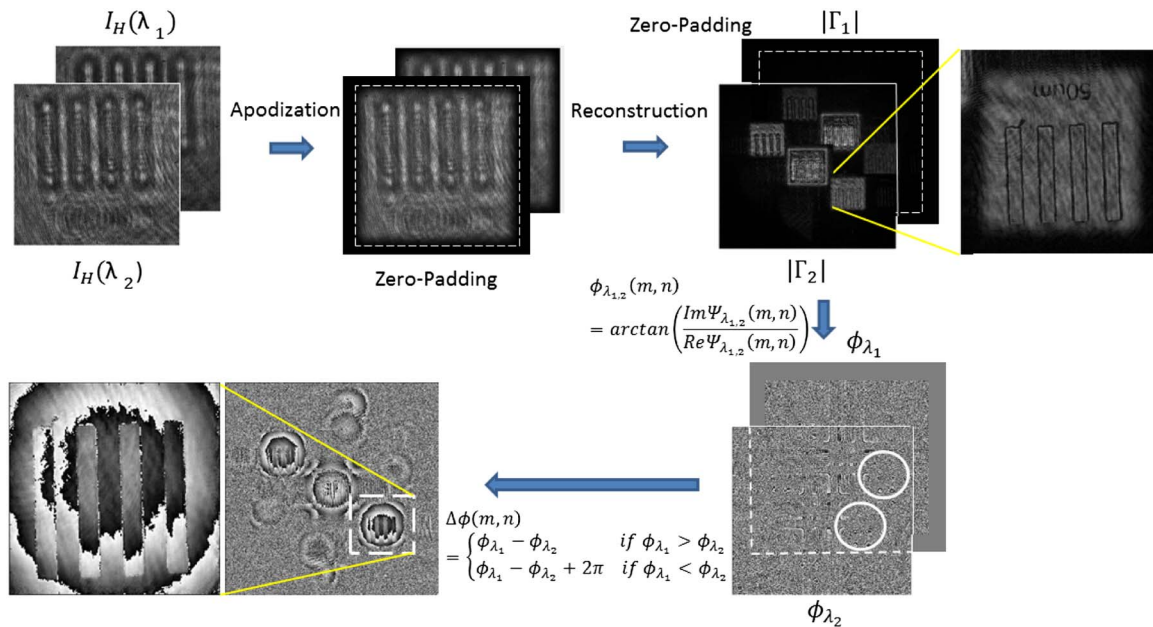


**Fig. 19.** Phase reconstruction steps in the multiwavelength approach. The first step is to perform apodization on the raw holograms, followed by zero-padding the holograms (one hologram is zero-padded prior to reconstruction, and the second hologram is zero-padded after reconstruction). The third step is to subtract the phases according to Eq. (20). The fourth step is to perform phase unwrapping, and the last step is to perform automatic aberration compensation.

Figure 14 shows the phase reconstruction process using a nontelecentric SW-DHM setup in reflection mode [similar to Fig. 4(a), but with intentional defocusing to make the setup nontelecentric].

The object used is a USAF 1951 resolution test target with a  $\sim 50$  nm reflective molybdenum film sputtered onto it, as shown in Fig. 14(a). The experiment parameters are as follows: wavelength  $\lambda = 488$  nm ( $\text{Ar}^+$  laser), a Nikon  $10\times/0.30$  infinity corrected MO, a Thorlabs ITL200 infinity-corrected microscope tube lens with a focal length of 16.5 cm, reconstruction distance  $d = 0.202$  m, magnification  $M \approx 10$ , and reference transverse angles  $k_{x0}/k_0 = 0.01307$ ,  $k_{y0}/k_0 = 0.01305$ . It should be noted that because of the nontelecentric setup, it is very difficult to obtain such precise parameter measurements in the laboratory. Typically, approximate measurements are made and then varied slightly during numerical reconstruction to yield the “best focus” image. In this nontelecentric setup ( $d_f \neq f_i$ ), the reconstructed wrapped phase shown in Fig. 14(b) contains spherical and higher order aberrations. Figure 14(c) shows the unwrapped phase, where the object patterns are shown lying on a spherical phase due to the MO. Note that maximum phase is approximately 48 rad, corresponding to the eight  $2\pi$  phase jumps shown in Fig. 14(b). As described in Section 2.F, the Zernike surface fitting model was employed to cancel the spherical phase due to the MO as well as the other higher order aberrations, with the result shown in Fig. 14(c).

### B. SW-DHM Using a Telecentric Setup (SW-TDHM)

In this section the SW-TDHM configuration will be employed for the phase reconstruction process, as shown in Fig. 15. In a telecentric arrangement, the spherical phase due to the MO is

completely eliminated and the reconstructed object phase is shown in Fig. 15(a). From the 3D profile distribution shown in Fig. 15(b), we can see that other higher order aberrations embedded in the total phase still exist. The measured phase

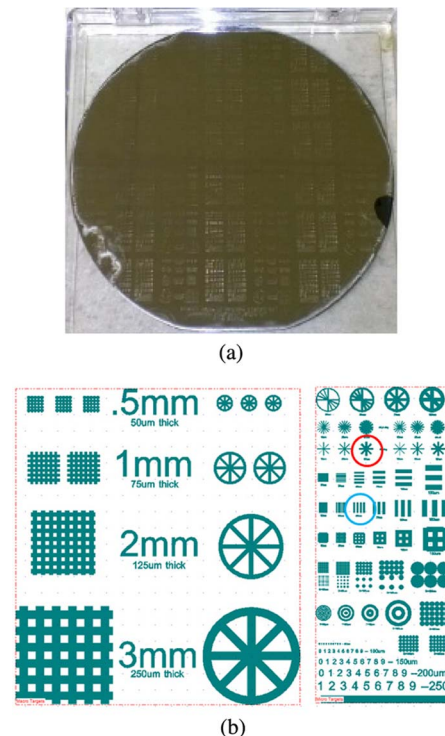


**Fig. 20.** (a) The fabricated object and (b) custom-fabricated lithography mask for generating microscale PMMA objects on silicon.

values were converted to height using Eq. (9a). The aberration compensation is performed using surface fitting with the Zernike model, and the 3D profile after aberration cancellation is shown in Fig. 15(c).

Figure 16 is a zoomed version of Fig. 15(c), where the vertical height and the transverse dimensions of the USAF 1951 resolution test target at group 4 element 3 is clearly marked.

The measured height values shown in Fig. 17(a) using an Ambios XP2 stylus profilometer match the measured heights shown in Fig. 17(b) over the same area to within the error due to surface roughness, which is  $\pm 7.5$  nm. Figure 17(b) shows a comparison between the measured height in nontelecentric (red) and telecentric (blue) setups, respectively. Notice that the standard deviation error in height using the DHM technique is ( $\pm 20$  nm) which is noisier than the Ambios (and has poorer lateral resolution) because of speckle noise. This error can be easily mitigated by averaging several holograms to reduce the speckle noise, and that brings down the standard deviation of error to match the profilometer measurement.

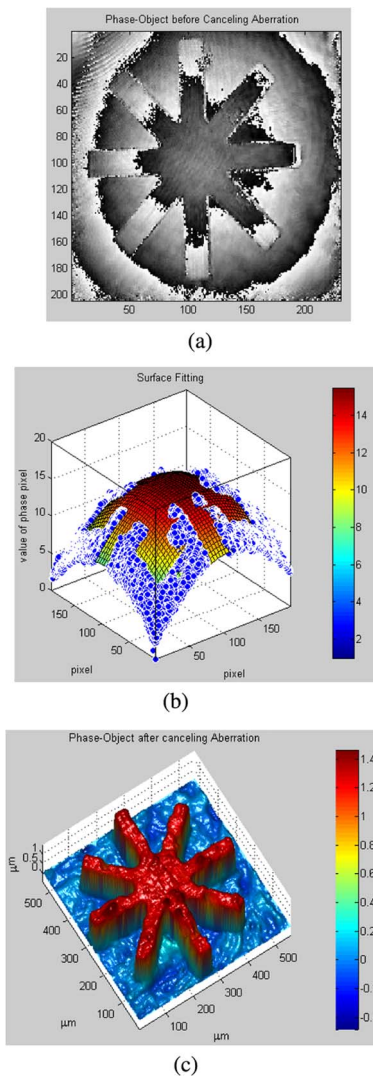


**Fig. 21.** Reconstructed phase using the MW-DHM nontelecentric setup: (a) wrapped phase, (b) 2D surface fitting, and (c) 3D height profile after canceling aberrations.

Another experiment using the SW-TDHM configuration of Fig. 4(b) is performed to find the 3D profile of the plano-convex parabolic microlens array, similar to that shown in Fig. 13(a). Figure 18(a) shows the reconstructed wrapped phase. Figure 18(b) shows the unwrapped reconstructed 3D profile after automatic aberration cancellation. Figure 18(c) shows the 3D profile obtained using the transport of intensity equation (TIE), with dashed white and blue lines representing different profile measurements [23,36]. Figure 18(d) shows the geometric explanation of the sample showing that the profile height along the blue line is  $s_1 = r - \sqrt{r^2 - \frac{p_1^2}{4}} = 1.3 \mu\text{m}$ . Since half of the dimension along the white diagonal line is  $p_2 = \sqrt{2}p_1$ , the profile height is  $s_2 = r - \sqrt{r^2 - \frac{p_2^2}{2}} = 2.6 \mu\text{m}$ . Comparison between the TIE and SW-DHM techniques along the dashed white line and the dashed blue line are shown in Figs. 18(e) and 18(f), respectively.

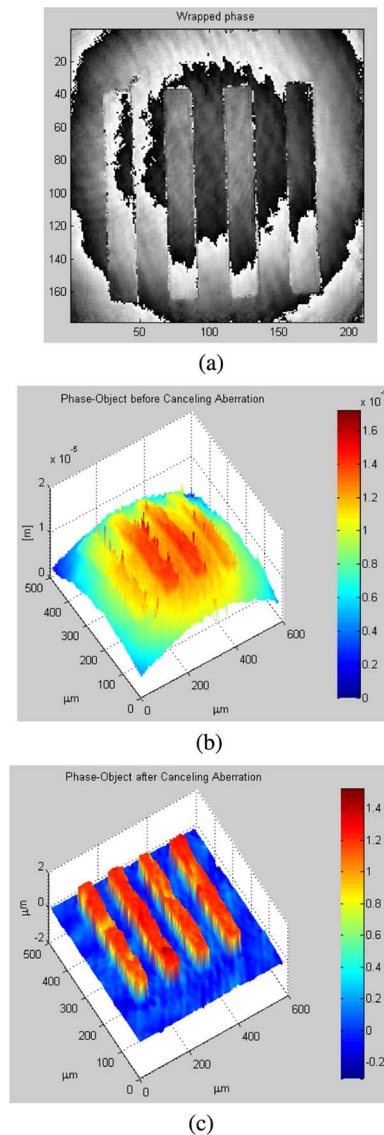


**Fig. 22.** Reconstructed phase using the MW-TDHM setup: (a) wrapped phase, (b) 3D height profile with aberration, and (c) 3D height profile after canceling aberrations.



### C. MW-DHM Using a Nontelecentric Setup

In this section, we obtain experimental results using a MW-DHM nontelecentric setup, as shown in Fig. 4(a), where we intentionally defocused the telecentric system to make it nontelecentric ( $C \neq 0$ ). The two wavelengths used in the experiment are  $\lambda_1 = 514$  nm and  $\lambda_2 = 488$  nm (Ar<sup>+</sup> laser), resulting in a synthetic wavelength:  $\Lambda = 9.647$   $\mu\text{m}$ . Figure 19 briefly illustrates the 3D phase reconstruction process using MW-DHM (see Section 3).

A custom-fabricated object was used, which consists of several transmissive photoresist (PMMA) patterns covered with a 30 nm of aluminum layer via vapor deposition on a silicon wafer, as shown in Fig. 20(a). The patterns under study are a set of four rectangular bars, each 50  $\mu\text{m}$  in width, and a star-shaped pattern with the same bar width, identified by the blue and red circles in Fig. 20(b), respectively. In the MW process, two holograms are recorded sequentially. Then, apodization is applied on the intensity holograms to eliminate the oscillations, as described in Section 2.E. The intensity and phase are then reconstructed using Eqs. (11a) and (11b), where  $k_{x0} = k_{y0} = 0$ , and the reconstructed distance  $d = 0.202$  m. The wrapped phase  $\Delta\phi(m, n)$  is calculated by subtraction of the two phases corresponding to the two wavelengths, as in Eq. (20). The MW reconstruction process is much easier than SW since MW needs little calibration because most of the aberrations are eliminated

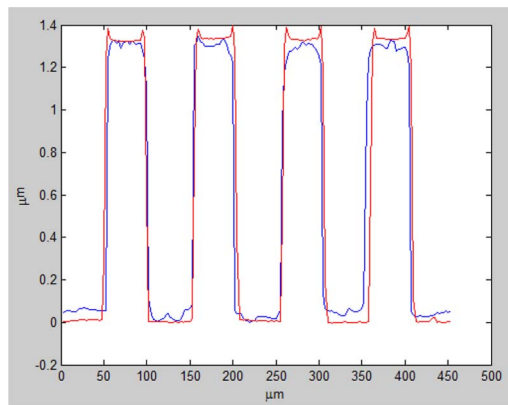


**Fig. 23.** Profilometer height measurement of the custom-made object (red), with the MW-TDHM height measurement (blue).

while performing the phase subtraction step during the reconstruction process.

Figure 21(a) shows the wrapped reconstructed phase of the object shown in Fig. 20 (red circle) using the MW-DHM setup. The reconstructed phase suffers from phase aberration. This phase aberration is caused partly by chromatic aberration in the optical system (defocusing effect) and partly caused by nontelecentricity. It is worth noting that due to the nontelecentric setup, there is a certain amount of parabolic fringes superposed on the object phase because of the different wavelengths, even though it is mostly eliminated by Eq. (20) when the two phases are subtracted from each other. Zernike polynomial surface fitting shown in Fig. 21(b) was applied to compensate for these aberrations, as shown in Fig. 21(c). Because the samples have very sharp edges, the jump in height causes some errors in the pixels on those edges. This can make the 2D unwrapping algorithm return the wrong results. A median filter was used to remove those error pixels to avoid this problem.

### D. MW-DHM Using a Telecentric Setup (MW-TDHM)

Figure 22 shows the reconstructed phase of the object shown in Fig. 20 (blue circle) using the MW-TDHM setup. Figure 22(a) shows the reconstructed wrapped phase. The reconstructed phase still suffers from residual chromatic aberration of the optical system. Figure 22(b) shows the 3D height profile with chromatic aberration, and Fig. 22(c) shows the 3D height profile after aberration cancellation using the Zernike polynomial model. We believe that while the fringes in Fig. 22(a) are due to chromatic aberration only, the fringes in Fig. 21(a) are due to a combination of defocusing due to nontelecentricity and chromatic aberration. However, more experimental data are needed to verify this claim because of the subtraction of the phases in the reconstruction algorithm, as shown in Eq. (20).

Figure 23 compares the accuracy of the MW-TDHM technique to that of a stylus profilometer. The red line is the profile measured from the profilometer and the blue line is from MW-TDHM. The height obtained is approximately 1.3  $\mu\text{m}$  and the width is 50  $\mu\text{m}$ .

Note that SW- and MW-TDHM configurations allow digital automatic aberration compensation for higher order aberrations and/or chromatic aberration easier to apply compared to nontelecentric configurations since the reconstruction parameters do not need to be measured with high precision.

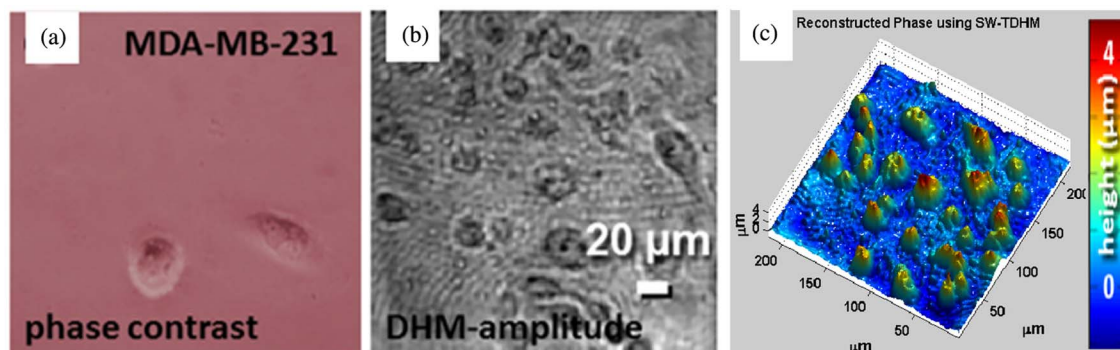


**Fig. 24.** DHM of cancer cells cultured on untreated glass coverslips. MDA-MB-231 cells in (a) phase contrast, (b) amplitude, and (c) phase height, using a telecentric DHM transmissive configuration.



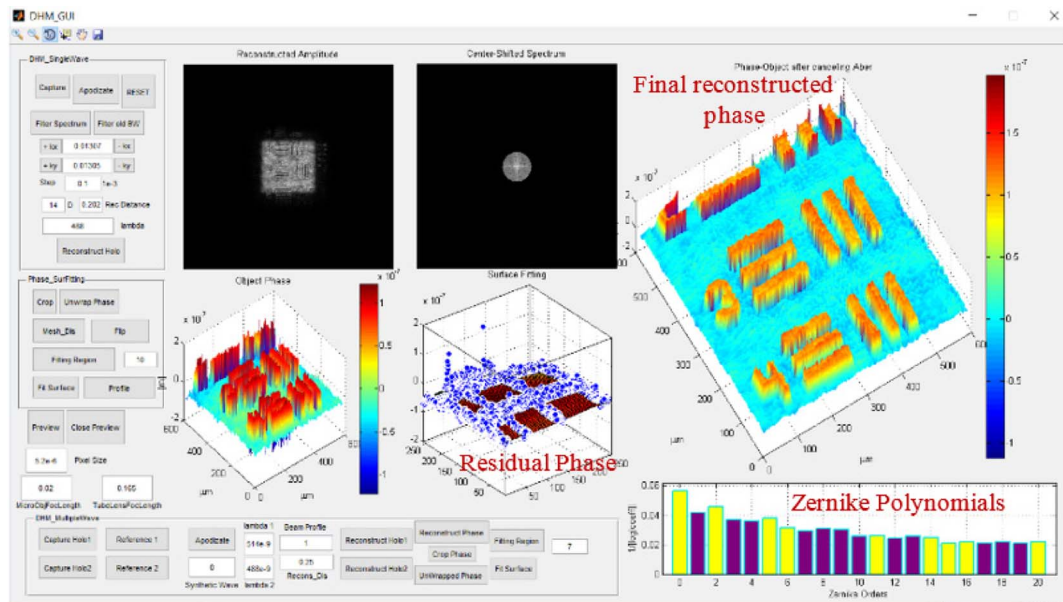


**Fig. 25.** Custom-designed GUI showing a SW-TDHM example in the reflection configuration. The object is a reflective object on a reflective substrate [see Fig. 14(a)].

### E. SW-DHM of Cancer Cells Using a Telecentric Setup

Cells from the highly invasive MDA-MB-231 breast cancer cell line were cultured and images were recorded using a phase-contrast microscope in Fig. 24(a). These cells were cultured in Petri dishes with untreated borosilicate glass bottoms for 48 h and then mounted with a second coverslip for DHM. Cancer cell amplitude and phase images were reconstructed from the recorded holograms, as shown in Figs. 24(b) and 24(c), respectively. The cells are slightly rounded due to low surface adhesion to the glass. It is important to note that a DHM in the

reflection configuration can be used for cells on gel surfaces. Dependent variables of local matrix 3D displacements during cell migration on the gel surface will be measured from DHM holograms in future work. Also, in a future experiment, we will use TDHM to record in real time (speed of the camera  $\sim 30$  fps), rapid fluctuations around migrating cancer cells undergoing cyclic loading to assist in determining the effects of local mechanical domains on cell migration and to identify cell responses to external force microloading. This will be a novel application of DHM where dynamic deformation can be deciphered from the captured holograms.

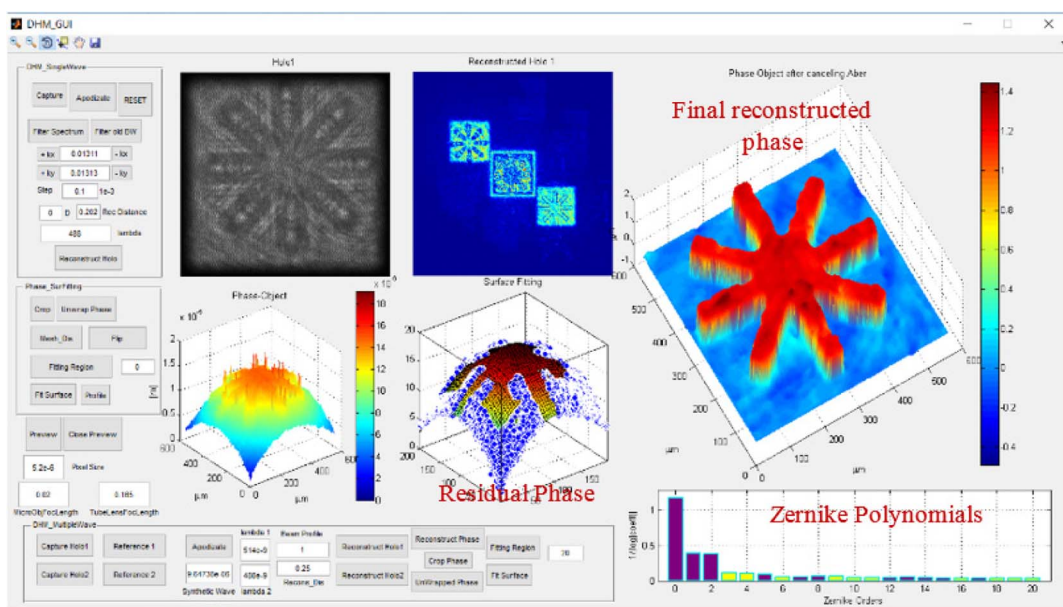


**Fig. 26.** Custom-designed GUI showing the MW-TDHM in the reflection configuration. The object is a reflected object on a reflective substrate [see Fig. 20(a)].

## F. Custom-Developed GUI

Figure 25 shows a custom-developed user-friendly graphical user interface for the SW-TDHM setup in reflection or transmission mode (see Fig. 4). The target object shown in the GUI is similar to that of Fig. 14(a). The MATLAB GUI is connected to a Lumenera LU100M CCD camera using a USB cable. The GUI is equipped with all the parameters needed to adapt to different CCD camera pixel sizes, laser wavelengths, reconstruction distances, and ore reflection versus transmission modes. In this example, the laser wavelength used is  $\lambda = 488$  nm, the CCD pixel size is  $5.2 \mu\text{m}$ , the reconstruction distance is  $d = 20.2$  cm, and the reconstructed height is around 120 nm. Also, the GUI is equipped with automatic aberration correction capability using the Zernike polynomial approximation of the residual phase. The telecentric technique has a lot of advantages since the reconstruction parameters needed to obtain the 3D phase information are hard to obtain with sufficient precision in a standard DHM setup.

Figure 26 shows a custom-developed user-friendly GUI for the MW-TDHM setup in reflection or transmission mode (see Fig. 4). The target in this experiment is the aluminum-coated (PMMA) object on a reflective Si background [see the element in the red circle in Fig. 20(a)]. The laser wavelengths used are  $\lambda_1 = 514.5$  nm and  $\lambda_2 = 488$  nm, the synthetic wavelength is  $\Lambda = 9.6 \mu\text{m}$ , the CCD pixel size is  $\Delta x = 5.2 \mu\text{m}$ , and the reconstruction distance is  $d = 20.2$  cm.

## 5. CONCLUSIONS

In this work, we discussed in detail several DHM systems based on single-wavelength and multiple-wavelength telecentric and nontelecentric optical configurations, in both transmission and reflection modes. We also discussed reconstruction algorithms, eliminating zero-order diffraction and the virtual image using spatial filtering, minimizing intensity and phase fluctuations using apodization, calibration processes, and different manual and automatic aberration compensation algorithms.

We conclude that in nontelecentric SW-DHM systems, reconstruction parameters must be accurately measured to obtain the 3D profile, which is often a tedious process. We also conclude that MW-TDHM systems have many advantages over SW-DHM systems because of the increase in dynamic range due to the synthetic wavelength, in which taller surface features, including discrete steps, can be measured without phase ambiguity, thus simplifying 2D unwrapping. Also, we noticed that MW-TDHM systems need little calibration because most of the aberrations are eliminated while performing the phase subtraction step during the reconstruction process.

Moreover, we compared optical and digital aberration compensation and concluded that telecentric configurations cannot compensate for higher order phase aberrations or for chromatic aberrations in the MW case. Hence, both optical aberration compensation as well as automatic aberration compensation using one of the 2D polynomial surface fitting models should be employed to obtain the best results. We also compared the measurements obtained from different DHM configurations and the measurements obtained using profilometry (for reflective substrates) or transport of intensity (for phase objects).

TDHM was also used to visualize MDA-MB-231 cultured breast cancer cells. Finally, custom-developed GUIs were developed to automate the reconstruction processes for all configurations.

## REFERENCES

1. B. Kemper, D. Carl, J. Schnekenburger, I. Bredebusch, M. Schäfer, W. Domschke, and G. von Bally, "Investigation of living pancreas tumor cells by digital holographic microscopy," *J. Biomed. Opt.* **11**, 034005 (2006).
2. N. Pavillon, J. Kühn, C. Moratal, P. Jourdain, C. Depeursinge, P. J. Magistretti, and P. Marquet, "Early cell death detection with digital holographic microscopy," *PLoS ONE* **7**, e30912 (2012).
3. J. Kühn, E. Shaffer, J. Mena, B. Breton, J. Parent, B. Rappaz, M. Chambon, Y. Emery, P. Magistretti, C. Depeursinge, P. Marquet, and G. Turcatti, "Label-free cytotoxicity screening assay by digital holographic microscopy," *Assay Drug Dev. Technol.* **11**, 101–107 (2013).
4. J. Kuhn, F. Montfort, T. Colomb, B. Rappaz, C. Moratal, N. Pavillon, P. Marquet, and C. Depeursinge, "Submicrometer tomography of cells by multiple-wavelength digital holographic microscopy in reflection," *Opt. Lett.* **34**, 653–655 (2009).
5. B. Rappaz, E. Cano, T. Colomb, J. Kühn, C. Depeursinge, V. Simanis, P. J. Magistretti, and P. Marquet, "Noninvasive characterization of the fission yeast cell cycle by monitoring dry mass with digital holographic microscopy," *J. Biomed. Opt.* **14**, 034049 (2009).
6. J. Kühn, E. Shaffer, J. Mena, B. Breton, J. Parent, B. Rappaz, M. Chambon, Y. Emery, P. Magistretti, C. Depeursinge, P. Marquet, and G. Turcatti, "Label-free quantitative cell division monitoring of endothelial cells by digital holographic microscopy," *J. Biomed. Opt.* **15**, 036009 (2010).
7. H. Sun, B. Song, H. Dong, B. Reid, M. A. Player, J. Watson, and M. Zhao, "Visualization of fast-moving cells in vivo using digital video microscopy," *J. Biomed. Opt.* **13**, 014007 (2008).
8. N. Pavillon, A. Benke, D. Boss, C. Moratal, J. Kühn, P. Jourdain, C. Depeursinge, P. J. Magistretti, and P. Marquet, "Cell morphology and intracellular ionic homeostasis explored with a multimodal approach combining epifluorescence and digital holographic microscopy," *J. Biophoton.* **3**, 432–436 (2010).
9. C. J. Mann, L. Yu, and M. K. Kim, "Movies of cellular and sub-cellular motion by digital holographic microscopy," *Biomed. Eng. Online* **5**(21), 1–10 (2006).
10. N. Warnasooriya, F. Joud, P. Bun, G. Tessier, M. Coppey-Moisand, P. Desbiolles, M. Atlan, M. Abboud, and M. Gross, "Imaging gold particles in living cell environments using heterodyne digital holographic microscopy," *Opt. Express* **18**, 3264–3273 (2010).
11. K. Jeong, J. J. Turek, and D. D. Nolte, "Fourier-domain digital holographic optical coherence imaging of living tissue," *Appl. Opt.* **46**, 4999–5008 (2007).
12. Y. Fang, C. Y. Y. Lu, C. N. P. Lui, Y. Zou, C. K. M. Fung, H. W. Li, N. Xi, K. K. L. Yung, and K. W. C. Lai, "Investigating dynamic structural and mechanical changes of neuroblastoma cells associated with glutamate-mediated neurodegeneration," *Sci. Rep.* **4**, 1–10 (2014).
13. R. John and V. P. Pandiyan, "An optofluidic bio-imaging platform for quantitative phase imaging of lab on a chip devices," *Appl. Opt.* **55**, A54–A59 (2016).
14. L. Williams, P. Banerjee, G. Nehmetallah, and S. Praharaj, "Holographic volume displacement calculations via multiwavelength digital holography," *Appl. Opt.* **53**, 1597–1603 (2014).
15. G. Nehmetallah and P. P. Banerjee, "Applications of digital and analog holography in 3D imaging," *Adv. Opt. Photon.* **4**, 472–553 (2012).
16. Y. Emery, E. Solanas, N. Aspert, A. Michalska, J. Parent, and E. Cucho, "MEMS and MOEMS resonant frequencies analysis by digital holography microscopy (DHM)," *Proc. SPIE* **8614**, 86140A (2013).
17. A. Asundi, *Digital Holography for MEMS and Microsystem Metrology* (Wiley, 2011).
18. G. Coppola, S. De Nicola, P. Ferraro, A. Finizio, S. Grilli, M. Iodice, C. Magro, and G. Pierattini, "Characterization of MEMS structures by microscopic digital holography," *Proc. SPIE* **4945**, 71–78 (2003).

19. E. CuChe, P. Marquet, and C. Depeursinge, "Simultaneous amplitude contrast and quantitative phase-contrast microscopy by numerical reconstruction of Fresnel off-axis holograms," *Appl. Opt.* **38**, 6994–7001 (1999).
20. M. Kim, "Principles and techniques of digital holographic microscopy," *SPIE Rev.* **1**, 018005 (2010).
21. U. Schnars and W. Jueptner, *Digital Holography* (Springer, 2005).
22. U. Schnars and W. Jueptner, *Digital Holography: Digital Hologram Recording, Numerical Reconstruction, and Related Techniques* (Springer, 2010).
23. G. Nehmetallah, R. Aylo, and L. Williams, *Analog and Digital Holography With MATLAB* (SPIE, 2015).
24. M. Arevalillo Herráez, D. R. Burton, M. J. Lalor, and M. A. Gdeisat, "A fast two-dimensional phase unwrapping algorithm based on sorting by reliability following a non-continuous path," *Appl. Opt.* **41**, 7437–7444 (2002).
25. E. CuChe, P. Marquet, and C. Depeursinge, "Aperture apodization using cubic spline interpolation: application in digital holographic microscopy," *Opt. Commun.* **182**, 59–69 (2000).
26. F. Montfort, F. Charrière, T. Colomb, E. CuChe, P. Marquet, and C. Depeursinge, "Purely numerical compensation for microscope objective phase curvature in digital holographic microscopy: influence of digital phase mask position," *J. Opt. Soc. Am. A* **23**, 2944–2953 (2006).
27. T. Colomb, F. Montfort, J. Kühn, N. Aspert, E. CuChe, A. Marian, F. Charrière, S. Bourquin, P. Marquet, and C. Depeursinge, "Numerical parametric lens for shifting, magnification, and complete compensation in digital microscopy," *J. Opt. Soc. Am. A* **23**, 3177–3190 (2006).
28. Z. W. Zhou, Y. Yingjie, and A. Asundi, "Study on aberration suppressing methods in digital micro-holography," *Opt. Lasers Eng.* **47**, 264–270 (2009).
29. T. Colomb, J. Kühn, F. Charrière, and C. Depeursinge, "Total aberrations compensation in digital holographic microscopy with a reference conjugated hologram," *Opt. Express* **14**, 4300–4306 (2006).
30. T. Colomb, E. CuChe, F. Charrière, J. Kühn, N. Aspert, F. Montfort, P. Marquet, and C. Depeursinge, "Automatic procedure for aberration compensation in digital holographic microscopy and applications to specimen shape compensation," *Appl. Opt.* **45**, 851–863 (2006).
31. E. Sánchez-Ortiga, P. Ferraro, M. Martínez-Corral, G. Saavedra, and A. Doblas, "Digital holographic microscopy with pure-optical spherical phase compensation," *J. Opt. Soc. Am. A* **28**, 1410–1417 (2011).
32. E. Sánchez-Ortiga, A. Doblas, M. Martínez-Corral, G. Saavedra, and J. García-Sucerquia, "Aberration compensation for objective phase curvature in phase holographic microscopy: comment," *Opt. Lett.* **39**, 417 (2014).
33. A. Doblas, E. Sánchez-Ortiga, M. Martínez-Corral, G. Saavedra, and J. García-Sucerquia, "Accurate single-shot quantitative phase imaging of biological specimens with telecentric digital holographic microscopy," *J. Biomed. Opt.* **19**, 046022 (2014).
34. G. Nehmetallah, "Multi-wavelength digital holographic microscopy using a telecentric reflection configuration," in *Topical Meeting in Digital Holography (DH) and 3D Imaging*, Shanghai, China, May 2015, paper DM3A.7.
35. G. Coppola, G. Di Caprio, M. Gioffré, R. Puglisi, D. Balduzzi, A. Galli, L. Miccio, M. Paturzo, S. Grilli, A. Finizio, and P. Ferraro, "Digital self-referencing quantitative phase microscopy by wavefront folding in holographic image reconstruction," *Opt. Lett.* **35**, 3390–3392 (2010).
36. T. Nguyen, G. Nehmetallah, D. Tran, A. Darudi, and P. Soltani, "Fully automated, high speed, tomographic phase object reconstruction using the transport of intensity equation in transmission and reflection configurations," *Appl. Opt.* **54**, 10443–10453 (2015).